

# Detecting Localized Density Anomalies in Multivariate Data via Coin-Flip Statistics

Sebastian Springer  
sspringe@sissa.it  
SISSA (IT)

Andre Scaffidi  
ascaffid@sissa.it  
SISSA (IT)

Maximilian Autenrieth  
ma2216@cam.ac.uk  
Cambridge (UK), Imperial (UK)

Gabriella Contardo  
gcontard@sissa.it  
UNG (SLO), SISSA (IT)

Alessandro Laio  
laio@sissa.it  
SISSA (IT)

Roberto Trotta  
rtrotta@sissa.it  
SISSA (IT), Imperial (UK)

Heikki Haario  
heikki.haario@lut.fi  
LUT (FI)

April 1, 2025

## Abstract

Detecting localized density differences in multivariate data is a crucial task in computational science. Such anomalies can indicate a critical system failure, lead to a groundbreaking scientific discovery, or reveal unexpected changes in data distribution. We introduce **EagleEye**, an anomaly detection method to compare two multivariate datasets with the aim of identifying *local* density anomalies, namely over- or under-densities affecting only localised regions of the feature space. Anomalies are detected by modelling, for each point, the ordered sequence of its neighbours' membership label as a coin-flipping process and monitoring deviations from the expected behaviour of such process. A unique advantage of our method is its ability to provide an accurate, entirely unsupervised estimate of the local signal purity. We demonstrate its effectiveness through experiments on both synthetic and real-world datasets. In synthetic data, **EagleEye** accurately detects anomalies in multiple dimensions even when they affect a tiny fraction of the data. When applied to a challenging resonant anomaly detection benchmark task in simulated Large Hadron Collider data, **EagleEye** successfully identifies particle decay events present in just 0.3% of the dataset. In global temperature data, **EagleEye** uncovers previously unidentified, geographically localised changes in temperature fields that occurred in the most recent years. Thanks to its key advantages of conceptual simplicity, computational efficiency, trivial parallelisation, and scalability, **EagleEye** is widely applicable across many fields.

## 1 Introduction

As data complexity and dimensionality continue to increase, discerning subtle differences between multivariate probability distributions has become crucial in computational science. Anomaly detection—the identification of rare but significant deviations from expected patterns—can unveil hidden structures, signal critical system failures, or lead to groundbreaking discoveries. Developing robust methods capable of capturing subtle differences in high-dimensional data necessitates innovative approaches for comparing and analysing complex distributions with precision and computational efficiency – a task that is often framed in terms of anomaly detection. Anomaly detection approaches are broadly categorised in *one-sample methods*, which operate solely on the dataset under scrutiny, and *two-sample methods*, which compare the data of interest (the ‘test set’) against a reference distribution (the ‘reference set’) to identify deviations indicative of anomalies. Our new method, called **EagleEye**, falls in the latter category.

In the landscape of two-sample methods, several techniques exist that work in high-dimensional spaces. Kernel-based tests, such as the Maximum Mean Discrepancy (MMD) [1], compare distributions by measuring distances in reproducing kernel Hilbert spaces. Energy statistics, including the Energy Distance [2, 3], quantify differences between distributions based on expected pairwise distances. Nearest neighbour methods, such as the Friedman–Rafsky test [4] and Schilling’s test [5], assess distributional differences by analysing proximity relations among data points. Among density estimation techniques, ANODE [6] detects anomalies by estimating probability densities with neural networks and computing likelihood ratios between test and reference datasets. CATHODE [7] extends this approach using conditional density estimation to capture complex feature correlations. Optimal transport methods, such as those based on the Wasserstein distance [8], compare distributions by calculating the minimal cost to transform one distribution into another. PQMass [9]

was recently proposed as a method to compare distributions using binary indicators—similar to **EagleEye** in spirit, but it relies on first partitioning the space before aggregating into a final score (or p-value), to assess the quality of generative models.

Despite these advancements, challenges remain in detecting anomalies in high-dimensional data without relying on complex models or intensive computational resources. Comprehensive literature reviews (for example, Ref. [10]) highlight the curse of dimensionality as a critical problem in anomaly detection, underscoring the need for scalable algorithms that can efficiently process large, high-dimensional datasets. Furthermore, most existing strategies predominantly target shifts in the overall data distribution—even if those shifts are extremely minor—rather than focusing on small, localized deviations. We instead focus on the detection of *localized* anomalies, which may affect only a tiny portion of the data space. These localized anomalies are particularly challenging to identify using conventional statistical methods when the two samples under scrutiny are nearly indistinguishable across most of the data space.

To address the above challenges, we introduce **EagleEye**, a density-based anomaly detection method for comparing two multivariate datasets with unknown distributions, focusing on detecting local density differences. **EagleEye**'s approach is grounded in a simple and intuitive process: flipping a fair coin. Consider two sets of data points—one representing the normal, expected distribution (the reference data), and another that may contain localized over- or underdensities of points (the test data). For each point in the test data, we examine its nearest neighbours within both reference and test sets. If the two datasets are generated from the same distribution (and therefore there are no anomalies), these neighbours will be a random mix from both datasets, much like expecting an equal number of heads and tails when flipping a fair coin many times. This randomness reflects the idea that there is no significant difference between the distributions of the two datasets in any given local region. However, if a local ensemble of points from the test set is anomalous—meaning, it significantly deviates from the reference data distribution—, points belonging to the test set will be disproportionately represented in its neighbourhood. This disrupts the expected distribution of neighbours—similar to flipping a coin multiple times and obtaining an unexpectedly large number of heads or tails, which might suggest the coin is biased. **EagleEye** quantifies this imbalance by “counting” the heads and tails in the local neighbourhood of each test point. By carrying out a statistical hypothesis test on whether the observed mix of neighbours deviates from what is expected from random chance (akin to the binomial distribution of coin flips), **EagleEye** can flag potentially anomalous points. Importantly, this test is performed individually for each point. This allows the identification of *local density anomalies*, which is the most important novelty of our approach. The identification of anomalies is then refined by iteratively eliminating from the test set the data points that make the coin-flip biased. In this way, **EagleEye** leverages the local structure of the data and adapts the scale of analysis to where the differences between the datasets are most significant, providing a flexible and robust framework for anomaly detection without relying on strict assumptions about the underlying data distribution. Note that **EagleEye** is not an outlier detection method, namely it will not detect a single outlier point as anomalous. Also, the aim is not to detect global deviations or trends, for which several powerful approaches are already available.

**EagleEye** focuses on small and localized deviations immersed in a vast data space in which the two samples are globally indistinguishable. Its formulation is intuitive, using straightforward concepts like local neighbourhoods and the analogy of flipping a coin. **EagleEye** ensures consistency and reproducibility since the method does not involve any random elements in computing the test statistic. Furthermore, running the analysis multiple times will always yield the same results. This determinism means findings are reliable and verifiable. Moreover, the method is efficient and scalable. Since each point in the test data can be analysed independently, the method allows for exact parallel processing. This means it can handle large datasets effectively without significant computational overhead. **EagleEye** also differs from competing methods because it does not require complex preliminary analysis or time-consuming training processes. Finally, **EagleEye** provides an estimate of the number of points contributing to any local density anomaly, as well as the number of points contributing only to the reference density. To our knowledge, **EagleEye** is therefore the only fully unsupervised method that can locally estimate the signal-to-background ratio for multiple density anomalies in a dataset, without relying on kernel-based approaches that implicitly encode assumptions about the data distribution.

## 2 Methodology

**EagleEye** is composed of three conceptually simple and computationally inexpensive steps: First, we flag putative anomalous points based on their anomaly score value, based on the coin-flip statistics (section 2.1). Second, we isolate a sample of points representative of the density anomaly by iteratively pruning the points with highest anomaly scores, until no detectable anomalies are left, leaving us with approximately equalized densities between test and reference sets (section 2.2). Thirdly, we identify the subset of points that coexists in the region of features space where a significant density anomaly resides, using a multimodal process of repêchage (section 2.3). Lastly, we demonstrate how to estimate the irreducible background, as well as signal purity, in any of potentially multiple local density anomalies (section 2.4). Each of these steps are detailed in the following subsections.

### 2.1 Flagging of putative anomalous points

Let  $\mathcal{X} = \{X_1, X_2, \dots, X_{n_{\mathcal{X}}}\}$  and  $\mathcal{Y} = \{Y_1, Y_2, \dots, Y_{n_{\mathcal{Y}}}\}$  be two independent samples drawn from  $d$ -variate distributions. We call the sets  $\mathcal{X}$  and  $\mathcal{Y}$  *reference* and *test* respectively. We denote the combined set  $\mathcal{U} = \mathcal{X} \cup \mathcal{Y}$ . For each point  $Y_i \in \mathcal{Y}$ , define  $\mathcal{N}_{\bar{k}}(Y_i) \subseteq \mathcal{U}$  to be its  $\bar{k}$ -nearest neighbors, using an appropriate distance metric (e.g., Euclidean). Some of these neighbors will lie in  $\mathcal{Y}$  and others in  $\mathcal{X}$ . We encode this membership in a binary sequence

$$\mathbf{b}_i = (b_i^1, b_i^2, \dots, b_i^{\bar{k}}),$$

where

$$b_i^k = \begin{cases} 0, & \text{if the } k\text{-th neighbor of } Y_i \text{ is in } \mathcal{X}, \\ 1, & \text{if the } k\text{-th neighbor of } Y_i \text{ is in } \mathcal{Y}. \end{cases}$$

Under the null hypothesis that  $\mathcal{X}$  and  $\mathcal{Y}$  are drawn from the same distribution, each  $b_i^k$  can be modeled as a Bernoulli random variable with success probability

$$\hat{p} = \frac{n_{\mathcal{Y}}}{n_{\mathcal{X}} + n_{\mathcal{Y}}}.$$

In the specific case where  $n_{\mathcal{X}} = n_{\mathcal{Y}}$ , we have  $\hat{p} = 0.5$ , and the sequence  $\mathbf{b}_i$  behaves analogously to a series of coin tosses.

To probe deviations from the Bernoulli assumption, we define the sum of  $K$  independent Bernoulli trials as

$$B(i, K) = \sum_{k=1}^K b_i^k.$$

Under the null hypothesis,

$$B(i, K) \sim \text{Binomial}(K, \hat{p}).$$

For each observed value  $B_{\text{obs}}(i, K)$ , we compute the right-tail  $p$ -value and define the corresponding statistic as

$$\Upsilon(i, K) := -\log(\text{pval}(B_{\text{obs}}(i, K))),$$

where the negative logarithm ensures numerical stability and facilitates interpretation.

Finally, the anomaly score for each point  $Y_i$  is defined as the maximum value of  $\Upsilon(i, K)$  over all neighborhood ranks  $K$  up to a maximum rank  $K_M$ :

$$\Upsilon_i := \max_{K \leq K_M} \Upsilon(i, K) = \max_{K \leq K_M} \left\{ -\log(\text{pval}(B_{\text{obs}}(i, K))) \right\}. \quad (1)$$

This formulation enables us to identify the most anomalous behaviour by selecting the maximum  $p$ -value-derived statistic over all considered neighbourhood sizes.

Larger values of  $K_M$  are particularly advantageous for detecting anomalies in high-dimensional settings and/or densely sampled feature spaces. Indeed, at small neighbourhood sizes data can be dominated by noise. In practice, however, we allow  $K_M$  to be at most 5% of the total data size (See Supp. Inf. for further details). For very large datasets ( $\gtrsim 10^5$  points),  $K_M$  may be reduced to mitigate computational cost.

In the first step of our procedure (Figure 1, panel a.) we flag points with an unexpectedly large value of the anomaly score  $\Upsilon_i$  (under the null hypothesis) as potentially belonging to a density anomaly:

$$\mathcal{Y}^+ := \{Y_i \in \mathcal{Y} \mid \Upsilon_i \geq \Upsilon_+^*\}, \quad (2)$$

where the value of the *critical threshold*  $\Upsilon_+^*$  hyperparameter is chosen such that the probability of obtaining a  $\Upsilon_i$  value exceeding it, based on sequences of  $K_M$  independent Bernoulli trials, is sufficiently low. As a default, we set this probability, which we denote  $p_{\text{ext}}$ , to  $p_{\text{ext}} = 10^{-5}$ . The data belonging to  $\mathcal{Y}^+$  will lead to what we call in Sec. 2.3 a  $\mathcal{Y}$ -*overdensity*. In the case of  $\hat{p} = 0.5$ , this has the intuition of being the sub-set of points in  $\mathcal{Y}$  that have significantly more neighbours belonging to  $\mathcal{Y}$  than to  $\mathcal{X}$ . In the supplementary information (Supp. Inf.) we present the stability of our algorithm with respect to moderate changes in the values of the two hyperparameters,  $K_M$  and  $\Upsilon_+^*$ .

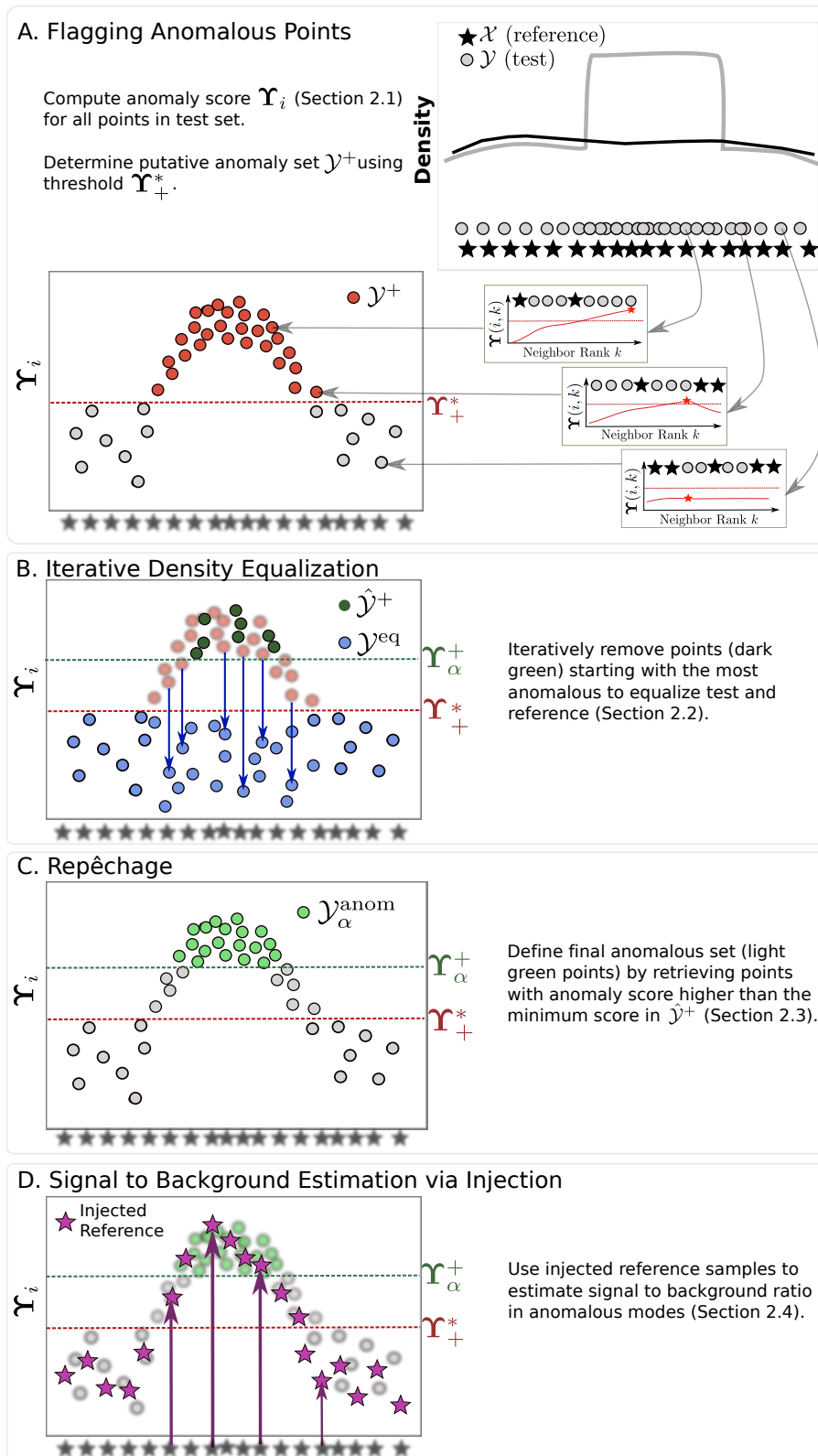


Figure 1: Sketch illustrating the conceptual steps in the **EagleEye** density anomaly detection methodology detailed in the text in Sec. 2.1 (sub-panel a.), Sec. 2.2 (sub-panel b.), Sec. 2.3 (sub-panel c.) and Sec. 2.4 (sub-panel d.). In each sub-panel, the plot on the left represents anomaly score (vertical axis) against feature space location of samples. For this cartoon, the anomaly is a top-hat overdensity (grey density in the top right panel).

This procedure is repeated by interchanging the roles  $\mathcal{Y} \leftrightarrow \mathcal{X}$ , which leads to the identification of an  $\mathcal{X}$ -*overdensity*. This leads to the definition

$$\mathcal{X}^+ := \{X_i \in \mathcal{X} \mid \Upsilon_i \geq \Upsilon_-^*\}, \quad (3)$$

where  $\Upsilon_+^* = \Upsilon_-^*$  if the  $\mathcal{X}$  and  $\mathcal{Y}$  have the same size ( $n_{\mathcal{X}} = n_{\mathcal{Y}}$ ). We emphasize that an *overdensity* in  $\mathcal{X}$  corresponds to an *underdensity* in  $\mathcal{Y}$ .

## 2.2 Pruning via iterative density equalization (IDE)

While points representative of a density anomaly are characterized by large  $\Upsilon_i$ , points in the vicinity of a significant density anomaly (but not contributing to it) can also acquire an inflated  $\Upsilon_i$  value, as a consequence of the binary sequence  $\mathbf{b}_i$  hitting an anomaly for sufficiently large  $K$  values, as illustrated in Figure 1, panel a. Therefore, the two sets  $\mathcal{X}^+$  and  $\mathcal{Y}^+$  typically contain not only genuine representatives of the density anomaly, but also what could be referred to (at least qualitatively) as “false positives”. These are points that are flagged as anomalous only because they are located close to the portion of the feature space where a density anomaly is present.

To address this issue, in the second step of our method we perform a pruning of the sets of potentially anomalous points,  $\mathcal{X}^+$  and  $\mathcal{Y}^+$ , via *iterative density equalization* (IDE). The purpose of IDE is to isolate points that are genuine representatives of a density anomaly, from those that falsely contribute as described above.

IDE proceeds as follows (illustrated in Figure 1, panel b.): First consider the equalization of  $\mathcal{Y}$ -*overdensities*. We denote the eventual set of points that will have a greatly reduced fraction of false positives (and therefore be genuine representatives of the density anomalies) by  $\hat{\mathcal{Y}}^+ \subset \mathcal{Y}^+$ . One initializes the two sets  $\mathcal{Y}^{\text{eq}} = \mathcal{Y}$  and  $\hat{\mathcal{Y}}^+ = \emptyset$ , and then iteratively performs the following steps:

1. Compute  $\Upsilon_i$  for all  $Y_i$  in  $\mathcal{Y}^{\text{eq}}$ .
2. Identify the point  $Y_{i_{\max}}$  with the largest value of  $\Upsilon$ :  $i_{\max} = \text{argmax}_{i \in \mathcal{Y}^{\text{eq}}} \Upsilon_i$ .
3. Remove  $Y_{i_{\max}}$  and all its nearest neighbours (up to the next point belonging to  $\mathcal{X}$ ) from  $\mathcal{Y}^{\text{eq}}$ , adding them to the set  $\hat{\mathcal{Y}}^+$ .

The iterative procedure is terminated when no points  $Y_i \in \mathcal{Y}^{\text{eq}}$  have  $\Upsilon_i \geq \Upsilon_+^*$ , i.e., all anomalous points have been removed and the *equalized test set*  $\mathcal{Y}^{\text{eq}}$  is statistically indistinguishable from  $\mathcal{X}$ .

Once again, the IDE procedure is repeated by interchanging  $\mathcal{Y} \leftrightarrow \mathcal{X}$  in order to divide the set  $\mathcal{X}$  in two sets  $\mathcal{X}^{\text{eq}}$  and  $\hat{\mathcal{X}}^+$ . The two sets  $\mathcal{X}^{\text{eq}}$  and  $\mathcal{Y}^{\text{eq}}$  do not contain density anomalies by construction, whilst the two *pruned sets*  $\hat{\mathcal{Y}}^+ \subset \mathcal{Y}^+$  and  $\hat{\mathcal{X}}^+ \subset \mathcal{X}^+$ , contain only representatives of the density anomaly.

## 2.3 Repêchage

The final set of points which constitutes an anomaly in **EagleEye** is built by identifying all the points with a score  $\Upsilon_i$  higher than the scores of the points which are identified as anomalous in the IDE step (See Figure 1, panel c.).

In a typical anomaly detection task, multiple localized anomalies may be present. We assume that points belonging to  $\mathcal{Y}^+$  (or  $\mathcal{X}^+$ ) are sufficiently close to each other if they come from the same anomaly, and sufficiently distant if they come from different anomalies. To proceed, we cluster the points flagged as potentially anomalous in step 1, namely those in  $\mathcal{Y}^+$  and  $\mathcal{X}^+$ . For clustering, we adopt the Density Peaks Advanced approach [11] using the implementation in Ref. [12], with default parameters.

We define  $\mathcal{Y}_\alpha^+$  ( $\mathcal{X}_\alpha^+$ ) to be the subset of points in  $\mathcal{Y}^+$  ( $\mathcal{X}^+$ ) that share the same cluster label  $\alpha$ . The set of points associated with anomaly  $\alpha$  in  $\mathcal{Y}$  is then the set satisfying the condition:

$$\mathcal{Y}_\alpha^{\text{anom}} := \{Y_i \in \mathcal{Y}_\alpha^+ \mid \Upsilon_i \geq \Upsilon_\alpha^+\} \quad (4)$$

where

$$\Upsilon_\alpha^+ = \text{quantile} \left( \left\{ \Upsilon_i^+ : Y_i \in \hat{\mathcal{Y}}^+ \cap \mathcal{Y}_\alpha^+ \right\}, q \right), \quad (5)$$

where  $q = 0.01$  by default and is chosen to avoid the dependence on a single value of  $\Upsilon_i^+$  which may be spuriously low due to statistical fluctuations. The result  $\mathcal{Y}_\alpha^{\text{anom}}$  is what we denote the *repêchage* set, and is the set of points that coexists in the region of the feature space where a significant density anomaly resides. The set  $\bigcup_\alpha \mathcal{Y}_\alpha^{\text{anom}} \subset \mathcal{Y}$  ( $\mathcal{Y}$ -*overdensities*), and similarly the set  $\bigcup_\alpha \mathcal{X}_\alpha^{\text{anom}} \subset \mathcal{X}$  ( $\mathcal{X}$ -*overdensities*) are then the final results of our methodology. The set  $\bigcup_\alpha \mathcal{Y}_\alpha^{\text{anom}}$  has the straightforward interpretation of representing regions of feature space within the test set  $\mathcal{Y}$  which contain overdensities. The interpretation of  $\bigcup_\alpha \mathcal{X}_\alpha^{\text{anom}}$  is more nuanced and depends on the scientific context. In essence, these points form overdensities in the reference set  $\mathcal{X}$  when compared to the test set  $\mathcal{Y}$ , indicating that there is a scarcity (leading to underdensity) of points in the corresponding region of  $\mathcal{Y}$ . A concrete example of this behaviour is provided in Section 3.

## 2.4 Estimating the irreducible background via injection

After repêchage, the set  $\bigcup_{\alpha} \mathcal{Y}_{\alpha}^{\text{anom}}$  will inevitably contain points that are not anomalous, but that occur in the same feature space region of a density anomaly. For the case of  $\mathcal{Y}$ -overdensities, it is useful to consider that within the region of each anomaly  $\alpha$  the test set is an admixture of two components: (i) points belonging to a density anomaly, which we call *signal*, whose expected cardinality under the anomaly-generating process is  $S_{\alpha}$ ; and (ii) points originating from the same (unknown) distribution as the reference set, which we call *background points* (i.e., points that would be present even in the absence of an anomaly), whose expected cardinality is  $B_{\alpha}$ . In order to estimate the relative proportions of signal to background points in  $\mathcal{Y}_{\alpha}^{\text{anom}}$ , we introduce the following *injection scheme*: we inject individual samples from the reference set into the test set, thus creating a representative, traceable subset of non-anomalous points. The proportion of injected samples that is identified as anomalous by **EagleEye** provides an estimate of the *irreducible background*, i.e., the proportion of background points that are attributed to contributing to a density anomaly.

In practice, we move each point  $X_i \in \mathcal{X}$  individually to  $\mathcal{Y}$ , creating the temporary sets  $\mathcal{Y} \cup \{X_i\}$  and  $\mathcal{X} \setminus \{X_i\}$ ; we then recalculate the point's anomaly score and determine whether this value exceeds the threshold defined in Equation 2, in which case the point is flagged as a potential anomaly. This happens when the injected point is within, or in close proximity to, an actual anomaly in  $\mathcal{Y}$ . This procedure yields the set:

$$\underline{\mathcal{Y}}^+ = \left\{ X_i \in \mathcal{X} \mid \Upsilon_i \geq \Upsilon_+^* \text{, when } \mathcal{Y} = \mathcal{Y} \cup \{X_i\} \text{ and } \mathcal{X} = \mathcal{X} \setminus \{X_i\} \right\}. \quad (6)$$

Naturally, the number of points in  $\underline{\mathcal{Y}}^+$  increases if anomalies are in regions with higher background density.

For each anomaly  $\alpha$ , analogously to the anomalous set  $\mathcal{Y}_{\alpha}^{\text{anom}}$ , we define the *injected set*:

$$\mathcal{Y}_{\alpha}^{\text{inj}} := \left\{ X_i \in \underline{\mathcal{Y}}^+ \mid \Upsilon_i \geq \Upsilon_{\alpha}^+ \right\}. \quad (7)$$

The injected set  $\mathcal{Y}_{\alpha}^{\text{inj}}$  can be used to obtain a quantitative measure of the signal-purity ratio for an anomaly  $\alpha$ , as we show below in Equation 8. Its counterpart set,  $\mathcal{X}_{\alpha}^{\text{inj}}$ , represents underdense points in  $\mathcal{X}$  corresponding to a local overdensity in  $\mathcal{X}$ .

To quantify the presence of a signal over the background it is desirable to have an estimator for the *signal-purity*  $S_{\alpha}/(S_{\alpha} + B_{\alpha})$  [13, 14]. If the anomaly is found in a region of low background, then  $S_{\alpha}/(S_{\alpha} + B_{\alpha}) \sim 1$ , while a value  $S_{\alpha}/(S_{\alpha} + B_{\alpha}) \ll 1$  indicates that the anomaly is immersed in a region of large background. This can be estimated as follows (the derivation can be found in the Supp. Inf):

$$\frac{\widehat{S_{\alpha}}}{S_{\alpha} + B_{\alpha}} = \frac{|\mathcal{Y}_{\alpha}^{\text{anom}}| - \left( |\mathcal{Y}_{\alpha}^{\text{inj}}| \frac{(n_{\mathcal{Y}} - |\underline{\mathcal{Y}}^+|)}{(n_{\mathcal{X}} - |\underline{\mathcal{X}}^+|)} \right)}{|\mathcal{Y}_{\alpha}^{\text{anom}}|}. \quad (8)$$

This estimator can be interpreted as follows: The signal, represented by the numerator, is the total number of points identified as anomalous,  $|\mathcal{Y}_{\alpha}^{\text{anom}}|$ , minus the expected background contribution. The latter is estimated from injection procedure,  $|\mathcal{Y}_{\alpha}^{\text{inj}}|$ , as detailed above, scaled by an appropriate reweighting factor which accounts for the relative sizes of the background components in the test set and the reference set. A corresponding, counterpart for the derivation of a signal purity with respect to  $\mathcal{X}$ -overdensities can be analogously obtained by the interchange of  $(\mathcal{Y}_{\alpha}^{\text{anom}}, \underline{\mathcal{Y}}^+, n_{\mathcal{Y}}, \mathcal{Y}_{\alpha}^{\text{inj}}) \leftrightarrow (\mathcal{X}_{\alpha}^{\text{anom}}, \underline{\mathcal{X}}^+, n_{\mathcal{X}}, \mathcal{X}_{\alpha}^{\text{inj}})$  in Equation 8.

## 3 Results

### 3.1 Gaussian Density Anomalies in a Uniform Background

We generated two synthetic datasets, each containing 50,000 points in three dimensions. In the test dataset, 47,250 points are drawn from a uniform distribution, and 2,750 points are sampled from seven Gaussians to form seven  $\mathcal{Y}$ -overdensities. Each  $\mathcal{Y}$ -overdensity is defined by a unique center—selected to ensure sufficient spatial separation—and by a diagonal covariance matrix scaled by successive integers starting at 1. The individual  $\mathcal{Y}$ -overdensities consist of 50, 100, 200, 300, 500, 700, and 900 points, respectively. An analogous procedure is applied to the reference dataset. Here, 48,900 points are uniformly distributed, while 1,100 points form three Gaussians  $\mathcal{X}$ -overdensities. These anomalies are specified by their chosen centers and diagonal covariance matrices scaled in increasing order starting from 1, with 100, 300, and 700 points, respectively. In regions where these  $\mathcal{X}$ -overdensities occur, the test dataset exhibits a corresponding underdensity.

For this analysis, we set the maximum neighborhood rank to  $K_M = 500$ , corresponding to 1% of the data size, and select the critical threshold so that the probability of exceeding it under the null is  $p_{\text{ext}} = 10^{-5}$ . This yields a critical threshold of  $\Upsilon_{\dagger}^* = 14.04$ .

Figure 2 shows the steps and the outcome of the analysis. Panel A shows the background points and the anomalies added as described above. Panel B displays the points flagged as putative  $\mathcal{Y}$ -overdensities (orange) and  $\mathcal{X}$ -overdensities (violet). This visualization also highlights the phenomenon whereby non-anomalous points in the vicinity of a genuine anomaly (shown in Panel A) may be flagged in the first step due to the influence of nearby anomaly regions. Panels C and D illustrate the clustered anomalies following the application of Iterative Density Equalization (dark green) and multimodal repêchage (light green). We show overdensities on the left, and underdensities on the right, as they are obtained in two separate passes of **EagleEye**. Panels E and F present the  $\Upsilon_i$  distribution, where the black line shows the null distribution obtained from multiple sequences of  $K_M$  independent Bernoulli trials; the gray histogram gives the distribution for the test set  $\mathcal{Y}$ , showing in red points belonging to the flagged anomalies set,  $\mathcal{Y}^+$ . The dark green histogram represents the scores for points in the pruned set,  $\hat{\mathcal{Y}}^+$ , while the light green histogram shows the distribution for the clustered anomaly set,  $\mathcal{Y}_{\alpha}^{\text{anom}}$ . Finally, the blue histogram depicts the distribution of the equalized test set,  $\mathcal{Y}^{\text{eq}}$ , which is remarkably close to the null distribution, indicating that the IDE procedure works appropriately.

Table 1 compares the number of points comprising each anomaly with the cardinalities of the reconstructed sets at each step of the analysis. These rows also show, in parenthesis, the number of signal points present after each stage.

	$\mathcal{Y}_{\alpha=0}$	$\mathcal{Y}_{\alpha=1}$	$\mathcal{Y}_{\alpha=2}$	$\mathcal{Y}_{\alpha=3}$	$\mathcal{Y}_{\alpha=4}$	$\mathcal{Y}_{\alpha=5}$	$\mathcal{Y}_{\alpha=6}$	$\mathcal{X}_{\alpha=0}$	$\mathcal{X}_{\alpha=1}$	$\mathcal{X}_{\alpha=2}$
<b>Signal:</b>	50 (50)	100 (100)	200 (200)	300 (300)	500 (500)	700 (700)	900 (900)	100 (100)	300 (300)	700 (700)
<b>Flagged:</b> $\mathcal{Y}^+$	91 (50)	167 (100)	326 (200)	507 (300)	770 (500)	1015 (699)	1320 (897)	227 (100)	608 (300)	862 (700)
<b>Pruned:</b> $\hat{\mathcal{Y}}^+$	52 (50)	69 (68)	153 (149)	230 (214)	359 (338)	526 (490)	669 (588)	89 (72)	295 (290)	702 (699)
<b>Repêchage:</b> $\mathcal{Y}_{\alpha}^{\text{anom}}$	62 (50)	93 (92)	211 (194)	308 (281)	537 (472)	688 (610)	1072 (861)	146 (99)	309 (300)	704 (700)
<b>Injected:</b> $\mathcal{Y}_{\alpha}^{\text{inj}}$	11	6	19	25	67	85	211	22	10	5
$\frac{S_{\alpha}}{S_{\alpha} + B_{\alpha}}$ :	0.83 (0.81)	0.94 (0.99)	0.91 (0.92)	0.92 (0.91)	0.88 (0.88)	0.88 (0.89)	0.81 (0.8)	0.85 (0.68)	0.97 (0.97)	0.99 (0.99)

Table 1: Support table for the example presented in fig. 2. The first seven columns correspond to the  $\mathcal{Y}$ -overdensities, while the last three columns represent the  $\mathcal{X}$ -overdensities. The first row shows the number of points added to generate each anomaly (with the subset remaining at each phase given in parentheses). The subsequent rows list, respectively, the numbers of elements flagged as putative anomalies, pruned by IDE, and obtained via multimodal repêchage. The second-to-last row indicates the cardinality of irreducible background points estimated by the injection procedure, while the last row gives the signal-purity estimator.

The two values presented provide insight into the trade-offs at each stage of the analysis. Notably, the flagged points include nearly all of the initially added points, but also capture a significant number of additional points from the surrounding space. The pruned set offers an estimate of the extra density in that region of the feature space. Finally, the repêchage set incorporates most of the initially added points, as well as points from the equalized set that occupy the same region of the feature space, but with fewer surrounding points compared to the flagged set.

This first controlled experiment demonstrates that our anomaly detection pipeline is capable of accurately identifying both overdensities and underdensities in a uniform background, thereby providing a robust foundation for its application to more complex datasets. We present this case in 3D to allow for suitable illustration of the density anomalies. We refer the reader to the Supp. Inf. for a study of robustness with respect to an increasing number of dimensions.

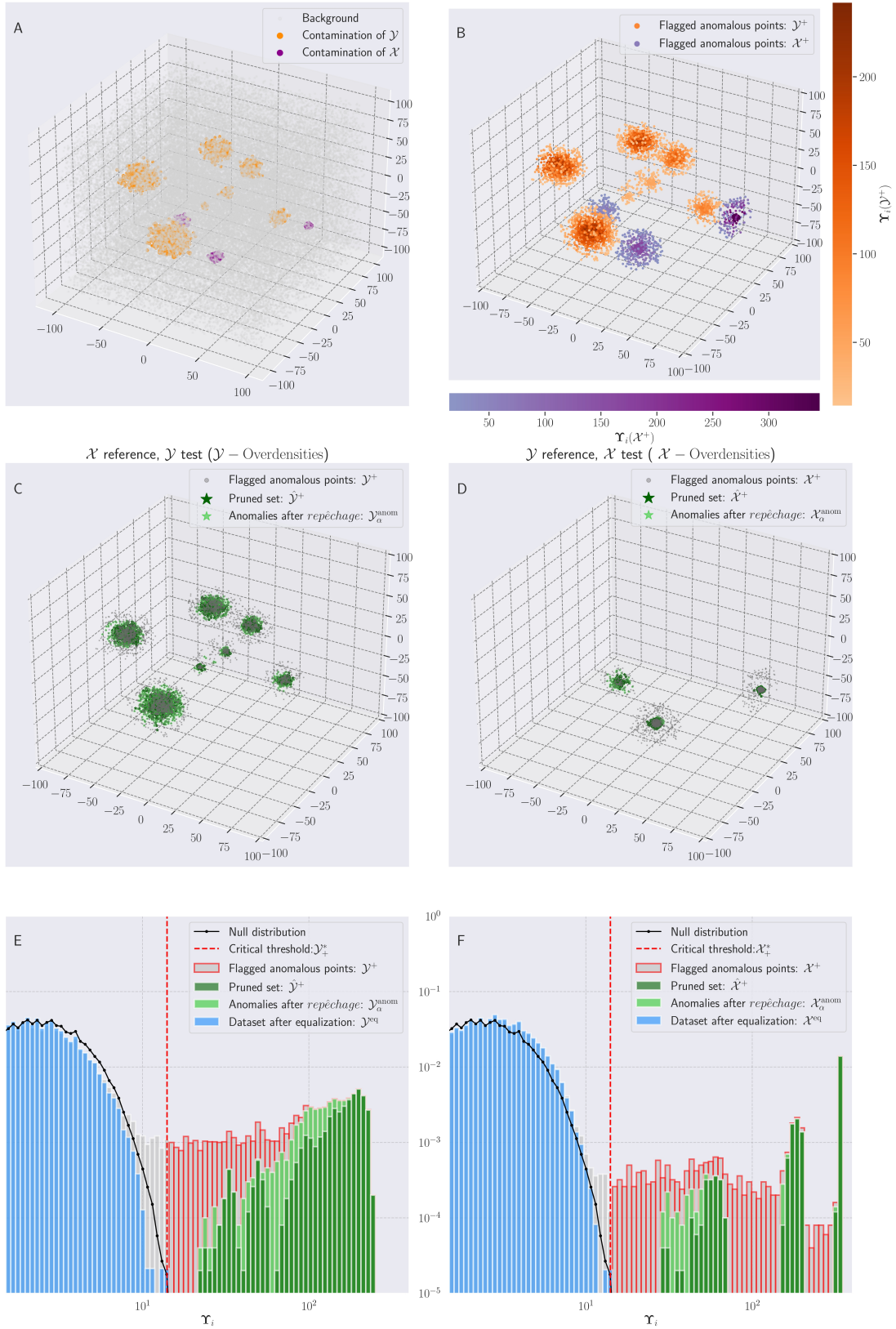


Figure 2: **EagleEye** detection of density anomalies within a uniform background. **(A)**: distribution of anomalies in feature space, showing overdensities (orange) and underdensities (violet). **(B)**: Points flagged as anomalous in the test set (warm orange shades) and in the reference set (cool violet shades). **(C)** and **(D)**: Local anomalies after Iterative Density Equalization (dark green) and multimodal repêchage (light green). On the left, overdensities, on the right, underdensities. **(E)** and **(F)**: Distribution of the anomaly score  $\Upsilon_i$  for sequences of Bernoulli trials (black, null distribution); the test set (gray), the pruned set (dark green); the clustered anomaly set (light green), and the equalized set (blue, matching the null distribution).



## 3.2 Resonant anomaly detection at the Large Hadron Collider

We next benchmark our approach in the field of particle physics, using synthetic data to evaluate **EagleEye**'s ability to detect a small signal stemming from the decay of extremely rare particles in a large background distribution. The Large Hadron Collider (LHC) [15] at CERN in Geneva, Switzerland, is arguably one of the most impressive scientific experiments in the world, associated with the discovery of the Higgs Boson in 2012 by the ATLAS and CMS collaborations [16–18]. The experiment continues to pursue the discovery of new physics beyond the standard model (BSM) at the teraelectronvolt (TeV) scale.

We employ **EagleEye** to search for signatures of short-lived particles decaying into hadrons, a type of analysis known as a “hadronic resonance search”, using the widely-studied LHC Olympics R&D dataset [19], created to replicate a signal which is difficult to identify using standard analysis methods [20]. This dataset provides  $10^6$  high-fidelity simulated events (data points) involving standard model processes, which serves as the reference data (background). The LHC Olympics R&D dataset also provides  $10^5$  signal events, containing a massive new particle whose decay products hadronise to produce jets. When a subset of these events are present on top of the background, it induces a subtle multi-modal density perturbation in feature space, which our analysis seeks to detect. The features consist of detector measurements of all particles in an event (padded to dimension 2100). Dimensionality reduction via jet clustering [21] is performed (details in Refs. [19, 22]), resulting in a 14-dimensional feature space for the two highest transverse momenta jets ( $j = 1, 2$ ): 3-momenta  $\mathbf{p}_j$ , invariant masses  $m_j$ , and N-jettiness variables [23]  $\tau_i^{(j)}$ , ( $i=1,2,3$ ). We observed that using all three components of  $\mathbf{p}_j$  leads to confounding neighbourhoods due to the degeneracy of the 3-momentum magnitude  $|p|_j$ , and that including the ratios  $\tau_2^{(j)}/\tau_1^{(j)} \equiv \tau_{21}^{(j)}$  and  $\tau_3^{(j)}/\tau_2^{(j)} \equiv \tau_{32}^{(j)}$ , following Refs. [22, 24], yields greater sensitivity. We therefore utilise the further reduced vector of  $d = 8$  features:

$$d = \left( |p|_1, |p|_2, \tau_{21}^{(1)}, \tau_{21}^{(2)}, \tau_{32}^{(1)}, \tau_{32}^{(2)}, m_1, m_2 \right). \quad (9)$$

We emphasise that, differently to most other methods, we do not apply any ‘signal region’ cuts — hard cuts that limit some feature values to regions of feature space expected to isolate the majority of the signal. This maintains the full distributional complexity of the data in a completely unsupervised manner. We subsample both the background and signal datasets, ensuring that the subsamples remain representative of their respective underlying distributions. This yields a test dataset of  $n_{\mathcal{Y}} = 500,000$  events, with injected signal events (i.e., anomaly points) constituting between 2% (10,000 events) and 0.30% (1,500 events). It is important to notice that the signal injection fractions used in this paper refer to the whole data space, while the fractions used in [7] are with respect to the signal region only – defined as events with a dijet invariant mass  $m_{jj}$  (effectively, a combination of the jet masses and 3-momenta) within the range  $m_{jj} \in [3.3, 3.7]$  TeV. The value of 0.3% represents the limit past which the performance of current best unsupervised methods significantly degrade [19, 25].

The signal exhibits a complex, multimodal distribution in the 8 dimensional feature space. We plot 2D histograms of the datasets for the three benchmark anomaly percentages in the top row of Figure 3, displayed as 2D histograms with gold scatter points, with varying density in each mode. The signal modes (i.e., overdensity anomalies) are most pronounced in the 2D space spanned by  $m_1, m_2$ , with the mode associated with the highest transverse momentum jet mass  $m_1$  having higher density due to enhanced kinematic statistics.

We choose the initial critical value  $\Upsilon_{\dagger}^* = 14$  with  $K_M = 1000$ , corresponding to the  $3.35 \times 10^{-5}$  quantile of the background-only distribution ( $\sim 4\sigma$ ). This was chosen to approximately maximise the estimated signal-purity using Eq. (8). We display the set of anomalous points after IDE ( $\hat{\mathcal{Y}}^+$ ) in the  $m_1, m_2$  plane in the second row of Figure 3, as well as the set  $\bigcup_{\alpha} \mathcal{Y}_{\alpha}^{\text{anom}}$ , after repêchage, indicating the corresponding minimum repêchage threshold  $\Upsilon_{\alpha}^+$  for which we choose  $q = 0$  in Equation 5 in order to maximally capture points in such a low anomaly density regime. The bottom row of Figure 3 shows the distributions of  $\Upsilon_i$  for the sets  $\mathcal{Y}^+$ ,  $\hat{\mathcal{Y}}^+$ ,  $\mathcal{Y}_{\alpha}^{\text{anom}}$  and  $\mathcal{Y}^{\text{eq}}$  for the three signal percentage benchmarks.

The estimated and true values of the signal-purity from Equation 8 are shown in Table 2. We additionally provide an estimate of the signal-to-background ratio  $S_{\alpha}/\sqrt{B_{\alpha}}$  as shown in Eq.11 in the Supp. Inf. This is an estimate of the statistical significance of a Poisson process, which is routinely used in particle physics experiments [26]. The “Total” signal-to-background, which is of primary scientific importance in LHC studies, aggregates the contributions from all repêchaged anomalies, indexed by  $\alpha$ . It is computed by substituting  $\mathcal{Y}_{\alpha}^{\text{anom}} \rightarrow \bigcup_{\alpha} \mathcal{Y}_{\alpha}^{\text{anom}}$  and  $\mathcal{Y}_{\alpha}^{\text{inj}} \rightarrow \bigcup_{\alpha} \mathcal{Y}_{\alpha}^{\text{inj}}$ , in Equations 8 and 11.

To our knowledge, no other method benchmarked on the LHC Olympics R&D dataset can estimate the signal purity in the multimodal overdense regions of the feature space, directly from their method in an unsupervised manner. While we cannot directly compare our analysis, which makes no use of pre-defined signal regions, to other approaches in the literature that do, we can nevertheless compare the true signal-to-background ratio (obtained using our knowledge of the labels of the anomalies added, which is not available in a real experiment) at the same signal percentages (see right plot of Figure 7 from Ref. [7]). Our results indicate that **EagleEye** performs comparably to CATHODE—which achieves a maximum ‘Total’  $S_{\alpha}/\sqrt{B_{\alpha}^{\text{Truth}}} \sim 5.7$  for a signal percentage of 0.3%, and outperforms ANODE and other semi-supervised methods with the same signal percentage. This

remarkable performance is achieved without the need for preselected signal regions or a reduction in the volume of the feature space as done with ANODE, CATHODE and other methods benchmarked on the LHC Olympics dataset [19]. For further caveats and details regarding the comparison of results obtained with **EagleEye** and the current pipelines, sensitivity studies and metrics used on LHC data, see the Supp. Inf.

	Anomaly percentage	$\Upsilon_{\alpha}^{+}$	$\widehat{\frac{S_{\alpha}}{\sqrt{B_{\alpha}}}}$	$\frac{S_{\alpha}}{\sqrt{B_{\alpha}}}$ Truth	$\widehat{\frac{S_{\alpha}}{S_{\alpha}+B_{\alpha}}}$	$\frac{S_{\alpha}}{S_{\alpha}+B_{\alpha}}$ Truth
<b>Total</b>	0.3%	<b>14.26</b>	<b>3.29</b>	<b>5.63</b>	<b>0.38</b>	<b>0.54</b>
$\alpha = 1$	0.3%	14.91	6.50	7.51	0.76	0.81
$\alpha = 2$	0.3%	14.26	0.39	2.75	0.07	0.41
<b>Total</b>	0.5%	<b>14.01</b>	<b>23.67</b>	<b>22.62</b>	<b>0.61</b>	<b>0.59</b>
$\alpha = 1$	0.5%	14.08	17.94	16.33	0.64	0.61
$\alpha = 2$	0.5%	14.01	15.42	15.78	0.58	0.59
<b>Total</b>	2%	<b>14.07</b>	<b>83.94</b>	<b>85.40</b>	<b>0.56</b>	<b>0.56</b>
$\alpha = 0$	2%	14.29	61.40	61.10	0.57	0.57
$\alpha = 1$	2%	14.07	56.85	60.03	0.54	0.56

Table 2: Estimated and true, per-anomaly ( $\alpha$ ) signal-purity and signal-to-background metrics for the three anomaly percentage benchmarks shown in Figure 3. True quantities are determined using the underlying simulation labels for points that are repêchaged as anomalous. The ‘Total’ values here, which are of primary scientific importance in LHC studies, consider the contribution from all repêchaged anomalies  $\alpha$  and are calculated by making the substitutions  $\mathcal{Y}_{\alpha}^{\text{anom}} \rightarrow \bigcup_{\alpha} \mathcal{Y}_{\alpha}^{\text{anom}}$  and  $\mathcal{Y}_{\alpha}^{\text{inj}} \rightarrow \bigcup_{\alpha} \mathcal{Y}_{\alpha}^{\text{inj}}$  in Eqns. 8 and 11.

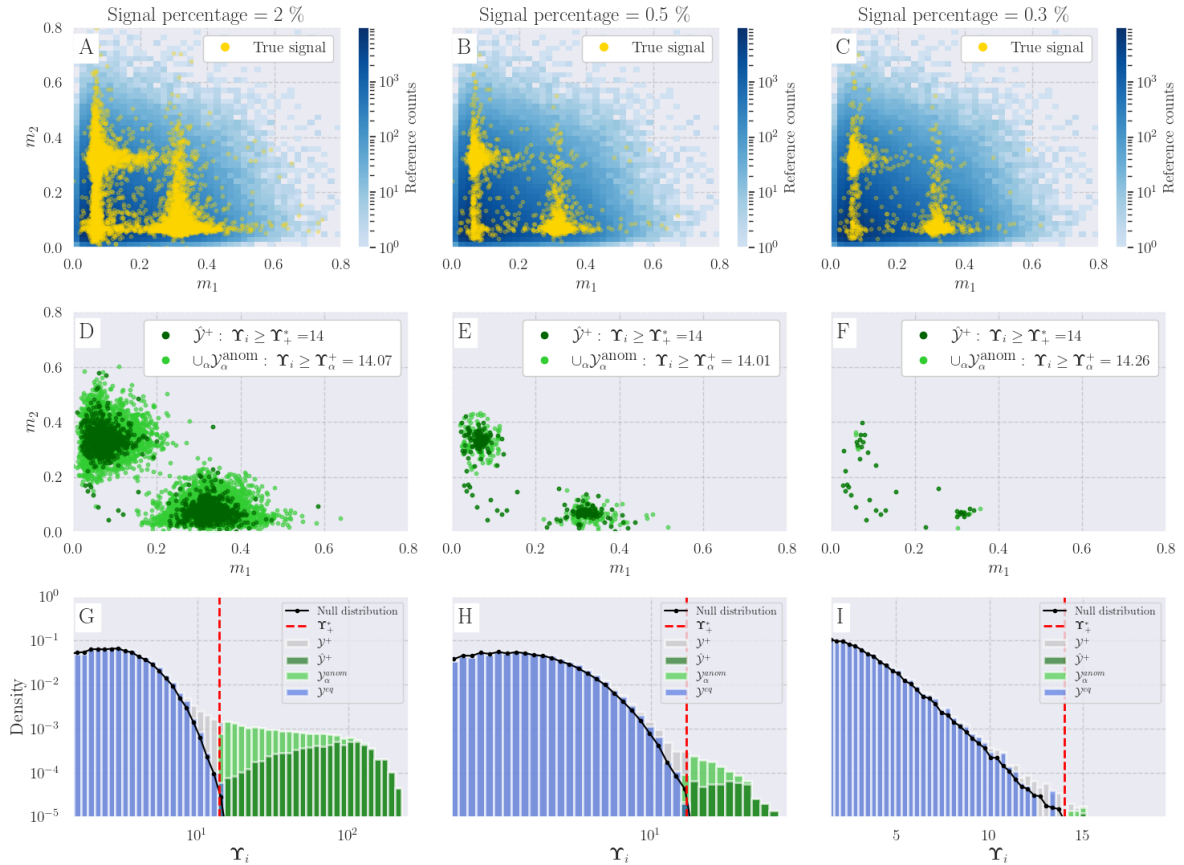


Figure 3: **Resonant anomaly detection on the LHC Olympics R&D dataset using EagleEye**. This figure demonstrates the application of EagleEye for resonant anomaly detection using the LHC Olympics R&D dataset. Each column corresponds to a different fraction of overdensity anomaly. The plots in the first two rows display 2D slices of the 8-dimensional feature space (in  $m_1$  and  $m_2$ , normalised units) that best illustrate the multimodal distribution of the signal events (anomalous data). **A–C** Histograms of the total reference (background) counts, with signal events overlaid as gold scatter points. **D–F** The sets  $\hat{\mathcal{Y}}^+$  (dark green) and  $\cup_{\alpha} \mathcal{Y}_{\alpha}^{\text{anom}}$  (light green) obtained using an initial threshold  $\Upsilon_i \geq \Upsilon_+^* = 14$  corresponding to a quantile of approximately  $4\sigma$  of the background-only  $\Upsilon_i$  distribution with  $K_M = 1000$ . **G–I** Histograms of the  $\Upsilon_i$  distributions on a logarithmic scale for: sequences of Bernoulli trials (black), the test set (gray), the pruned set  $\hat{\mathcal{Y}}^+$  (dark green), the repêchage set  $\mathcal{Y}_{\alpha}^{\text{anom}}$  (light green), and the equalized set  $\mathcal{Y}^{\text{eq}}$  (blue). The initial critical threshold  $\Upsilon_+^* = 14$  is indicated by a red dashed line.

### 3.3 Detecting Density Anomalies in Global Temperature Data

As a final example, we apply EagleEye to analyze daily average air temperature fields measured at 2 meters above sea level (Air2m) over the past 70 years. Our objective is to detect shifts in temperature patterns that have emerged or disappeared in recent years, potentially representing anomalies compared to historical patterns. We utilize data from the NCEP/NCAR Reanalysis 1 project [27], focusing on the Northern Hemisphere. To capture seasonal variations, we consider the winter (December–February; DJF) and summer (June–August; JJA) seasons separately.

The temperature field in this dataset is represented on a spatial grid with 37 latitudinal rows and 144 longitudinal columns, each spaced at intervals of  $2.5^\circ$ . To mitigate the systematic effects of global warming trends and instead capture variations in the recurrence rate of specific spatial temperature patterns, we de-trended and de-seasonalized the data. This was achieved by subtracting the corresponding seasonal average for each year separately, and then removing the seasonal cycle. Both computations were performed independently for each grid cell, with the seasonal cycle obtained as the average temperature across years on each corresponding calendar day.

Following the methodology described by Springer *et al.* [28], we analysed these data in longitudinal windows of  $60^\circ$  width. By moving the centre of the window, we span the entire Northern Hemisphere to investigate whether anomalies appear in specific regions. We divide the 72 years of data into three periods of 2130 days each: the earliest period (1951–1974) serves as the reference data, while the subsequent periods (1975–1998 and 1999–2022) are treated as two test sets.

Figure 4 presents the results of the analysis for the DJF (panels B, D, G, H) and JJA (panels A, C, E, F) seasons. In panels A, B, C, and D, the markers indicate the number of days, for each window

centered at the corresponding longitude, where  $\Upsilon_i > \Upsilon_+^* = 11.7$  ( $p_{\text{ext}} = 10^{-5}$ ) with  $K_M = 100$ . To assess the impact of using different reference periods, we conducted a sensitivity analysis by running **EagleEye** with reference sets constructed by shifting the start of the time window between 1950 and 1951, while keeping the total number of days in the reference dataset constant. The negligible standard deviations obtained from these shifted reference periods highlight the stability of the moving-window analysis results.

Inspection of the first four panels reveals a distinct seasonal pattern. During the JJA season (panels A and C), the predominance of violet colours indicates an overdensity in the reference set—implying that many temperature patterns observed in earlier periods have become less frequent over time. Conversely, in the DJF season (panels B and D), the dominance of orange colours signifies an overdensity in the test set, suggesting that certain temperature patterns have become more prevalent. Notably, the test set corresponding to the most recent period (1999–2022) exhibits a higher fraction of anomalous days compared to the earlier test period (1975–1998). This difference is particularly pronounced over the Atlantic sector during the DJF season, where a distinct peak appears only in the most recent period. In contrast, during the JJA season, two distinct peaks emerge over the Pacific and Atlantic sectors, with the more recent period displaying a slightly stronger signal.

Panels E–H illustrate the average temperature patterns corresponding to the days with the highest  $\Upsilon_i$  values and their ten nearest neighbours from the repêchage set  $\mathcal{Y}_\alpha^+$ . The color scale, ranging from  $-10^\circ\text{C}$  to  $10^\circ\text{C}$ , highlights the temperature configurations most affected by changes in the recurrence rate within these specific regions during the most recent test period. In particular, panel E corresponds to the  $\mathcal{X}^+$  set for a window centred at  $180^\circ$  (representing the Pacific peak observed in panel C), while panel F corresponds to  $\mathcal{X}^+$  for a window centred at  $30^\circ\text{W}$  (capturing the Atlantic peak in panel C). Panels G and H correspond to the  $\mathcal{Y}^+$  sets for windows centred at  $30^\circ\text{W}$  and  $20^\circ\text{W}$ , respectively, illustrating elements of the Atlantic peak in panel D. Panels G–H predominantly exhibit positive temperature anomalies within the window of interest, with particularly intense magnitudes over Greenland during DJF, whereas panels E–F include regions with both positive and negative anomalies.

Given the substantial fraction of anomalous days observed in geographically localized regions, further investigation into the specific temperature patterns driving these anomalies could enhance our understanding of evolving regional dynamics. We defer this detailed exploration to future work.

This results indicate that significant shifts in the recurrence of specific temperature patterns are localized in both space and season, underscoring the efficacy of **EagleEye** in capturing these subtle yet critical changes in climate dynamics.

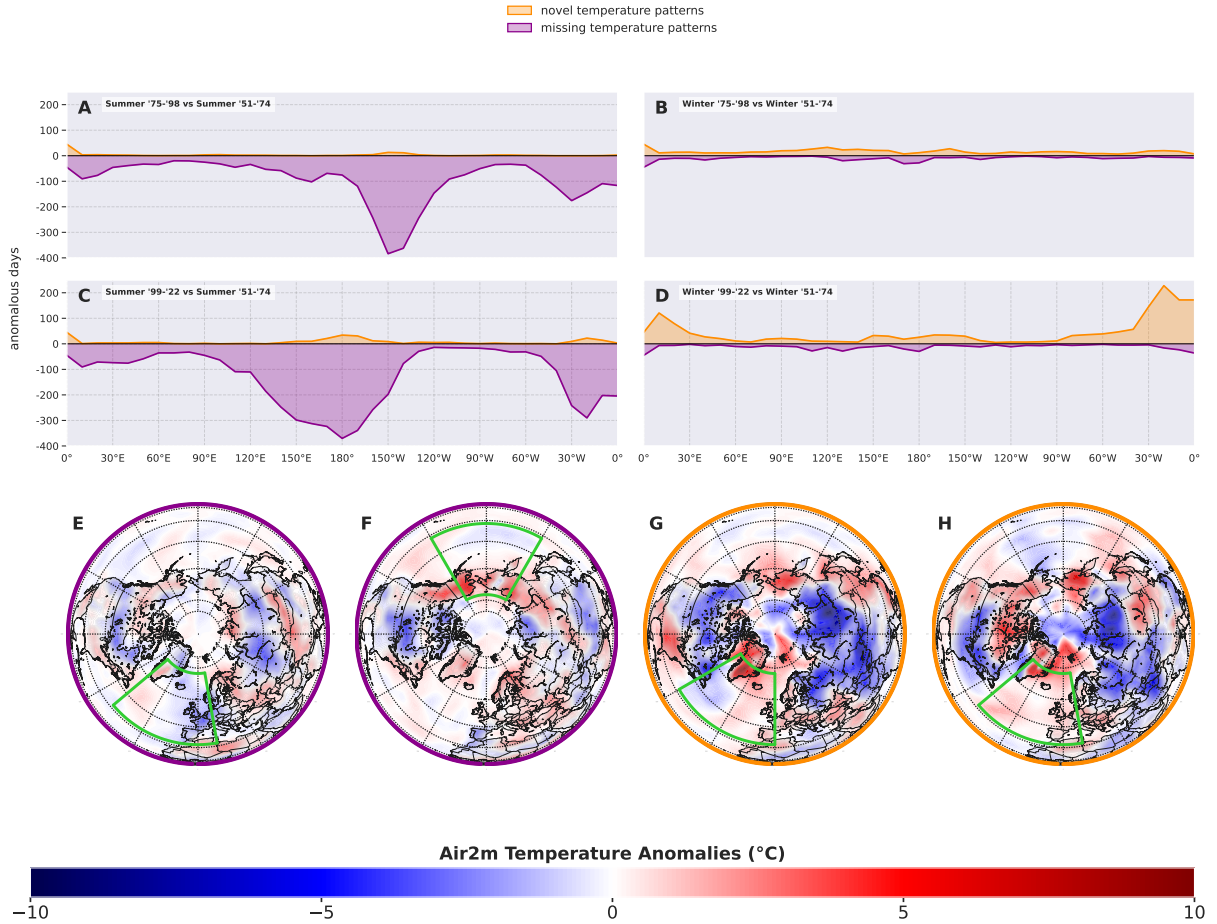


Figure 4: **Analysis of Air2m anomalies for the DJF and JJA seasons.** This figure demonstrates the application of *EagleEye* to detect shifts in temperature patterns over the past seventy years using global daily average air temperature fields measured at 2 m above sea level (Air2m). The analysis focuses on the Northern Hemisphere, with separate examinations for winter (DJF) and summer (JJA) seasons. **Panels A–D:** The number of anomalous days identified in the pruned set  $\hat{\mathcal{Y}}^+$  is shown for a moving  $60^\circ$  longitudinal window. Each of the three time periods comprises 2130 days. Negative values indicate  $\mathcal{X}$ -overdensities (i.e., regions where anomalies correspond to an overdensity in the reference set), which aids in readability; panels A and C correspond to JJA, while panels B and D correspond to DJF. A sensitivity analysis, performed by shifting the reference period, confirmed the robustness of these results (only the average is shown, as the variance was negligible). **Panels E–H:** These panels display the average de-trended and de-seasonalized Air2m anomalies for the day with the largest  $\Upsilon_i$  and its ten nearest neighbors from the repêchage set  $\mathcal{Y}_\alpha^+$ . For DJF, the central longitudes are  $30^\circ\text{W}$  and  $20^\circ\text{W}$  (panels G and H), while for JJA they are  $180^\circ$  and  $30^\circ\text{W}$  (panels E and F). Green boxes in each subplot delineate the regions used for the computations.

## 4 Conclusion

In this work, we have introduced **EagleEye**, a method for detecting localized density differences between two datasets. Leveraging the properties of a Bernoulli process and its connection to binomial statistics, **EagleEye** provides an algorithm for comparing two multivariate distributions within the local neighbourhood of each test point, without relying on the underlying distributions of the data. Its key advantages are conceptual simplicity, high computational efficiency, trivial parallelisability, scalability to moderately high-dimensional data and robustness to the characteristics of anomalies. Furthermore, its most important feature is its sensitivity to small anomalies in large data spaces with the ability to estimate the local and total signal-purity of anomalies in an unsupervised manner.

We demonstrated the effectiveness of **EagleEye** through experiments on both synthetic and real-world datasets. In controlled artificial data scenarios, **EagleEye** accurately detected anomalies, even when they were subtle and sparsely distributed. The method showed robustness across different anomaly characteristics and data volumes.

Applied to a benchmark resonant anomaly detection task in simulated LHC data, **EagleEye** identified rare particle decay events, leading to a successful detection of anomalies affecting just 0.3% of the dataset, without any prior assumption on the nature of the anomalous signal. This showcases the potential of our approach in high-energy physics applications. In the context of climate data analysis, **EagleEye** uncovered both the appearance of novel temperature patterns and the disappearance of other patterns over recent decades, thus highlighting regions experiencing accelerated changes in the overall weather dynamics, and providing valuable and localized insights into climate dynamics beyond general warming trends. The same approach can be extended to the Southern Hemisphere and/or applied to other other climate variables, such as precipitation, greenhouse gas concentrations, and surface radiation, to provide a more comprehensive and fine-grained understanding of climate change impacts across different regions and dimensions.

Future work will be devoted to combining our approach with dimensionality reduction techniques and neural network-based methods to identify the most informative dimensions for anomaly detection – a potential path to deploy **EagleEye** in extremely high-dimensional feature spaces.

Being entirely data format- and model-agnostic, our method is potentially applicable to a wide variety of fields, including finance (to identify fraudulent transactions, unusual trading patterns, and risks in investment portfolios), healthcare (for early disease detection, to monitor patient vital signs for irregularities, and to ensure data integrity in medical records), cybersecurity (to detect unusual network traffic, identify potential breaches, and monitor system behaviour for malicious activities), industry sensor data (with applications in predictive maintenance, early identification of equipment malfunctions, and in ensuring operational efficiency by monitoring production processes and environmental conditions), and betting (to uncover unusual betting patterns, detect potential match-fixing, and enhance the fairness and integrity of betting systems).

## References

- [1] Arthur Gretton, Karsten M. Borgwardt, Malte J. Rasch, Bernhard Schölkopf, and Alexander Smola. A kernel two-sample test. *Journal of Machine Learning Research*, 13(25):723–773, 2012.
- [2] Gábor J Székely, Maria L Rizzo, et al. Testing for equal distributions in high dimension. *InterStat*, 5(16.10):1249–1272, 2004.
- [3] Gábor J. Székely and Maria L. Rizzo. Energy statistics: A class of statistics based on distances. *Journal of Statistical Planning and Inference*, 143(8):1249–1272, 2013.
- [4] Jerome H. Friedman and Lawrence C. Rafsky. Multivariate generalizations of the wald-wolfowitz and smirnov two-sample tests. *The Annals of Statistics*, 7(4):697–717, 1979.
- [5] Mark F. Schilling. Multivariate two-sample tests based on nearest neighbors. *Journal of the American Statistical Association*, 81(395):799–806, 1986.
- [6] Benjamin Nachman and David Shih. Anomaly detection with density estimation. *Phys. Rev. D*, 101:075042, Apr 2020.
- [7] Anna Hallin, Joshua Isaacson, Gregor Kasieczka, Claudius Krause, Benjamin Nachman, Tobias Quadfasel, Matthias Schlaffer, David Shih, and Manuel Sommerhalder. Classifying anomalies through outer density estimation. *Phys. Rev. D*, 106:055006, Sep 2022.
- [8] Aaditya Ramdas, Nestor G. Trillos, and Marco Cuturi. On wasserstein two-sample testing and related families of nonparametric tests. *Entropy*, 19(2):47, 2015.
- [9] Pablo Lemos, Sammy Sharief, Nikolay Malkin, Laurence Perreault-Levasseur, and Yashar Hezaveh. Pqmass: Probabilistic assessment of the quality of generative models using probability mass estimation. *arXiv preprint*, 2024.
- [10] Lukas Ruff, Jens R. Kauffmann, Robert A. Vandermeulen, Grégoire Montavon, Klaus-Robert Müller, and Marius Kloft. A unifying review of deep and shallow anomaly detection. *Proceedings of the IEEE*, 109(5):756–795, 2021.
- [11] Maria d’Errico, Elena Facco, Alessandro Laio, and Alex Rodriguez. Automatic topography of high-dimensional data sets by non-parametric density peak clustering. *Information Sciences*, 560:476–492, 2021.
- [12] Aldo Glielmo, Iuri Macocco, Diego Doimo, Matteo Carli, Claudio Zeni, Romina Wild, Maria d’Errico, Alex Rodriguez, and Alessandro Laio. Dadapy: Distance-based analysis of data-manifolds in python. *Patterns*, page 100589, 2022.
- [13] R. Frühwirth and R. K. Bock. *Data analysis techniques for high-energy physics experiments*, volume 11. Cambridge University Press, 2000.
- [14] G. Cowan. *Statistical Data Analysis*. Oxford science publications. Clarendon Press, 1998.
- [15] Lyndon Evans and Philip Bryant. Lhc machine. *Journal of Instrumentation*, 3(08):S08001, 2008.
- [16] Peter W. Higgs. Broken symmetries and the masses of gauge bosons. *Physical Review Letters*, 13(16):508–509, 1964.
- [17] ATLAS Collaboration. Observation of a new particle in the search for the standard model higgs boson with the atlas detector at the lhc. *Physics Letters B*, 716(1):1–29, 2012.
- [18] CMS Collaboration. Observation of a new boson at a mass of 125 gev with the cms experiment at the lhc. *Physics Letters B*, 716(1):30–61, 2012.
- [19] Gregor Kasieczka, Benjamin Nachman, David Shih, Oz Amram, Anders Andreassen, Kees Benkenendorfer, Blaz Bortolato, Gustaaf Brooijmans, Florencia Canelli, Jack H Collins, Biwei Dai, Felipe F De Freitas, Barry M Dillon, Ioan-Mihail Dinu, Zhongtian Dong, Julien Donini, Javier Duarte, D A Faroughy, Julia Gonski, Philip Harris, Alan Kahn, Jernej F Kamenik, Charanjit K Khosa, Patrick Komiske, Luc Le Pottier, Pablo Martín-Ramiro, Andrej Matevc, Eric Metodiev, Vinicius Mikuni, Christopher W Murphy, Inés Ochoa, Sang Eon Park, Maurizio Pierini, Dylan Rankin, Veronica Sanz, Nilai Sarda, Urő Seljak, Aleks Smolkovic, George Stein, Cristina Mantilla Suarez, Manuel Szwec, Jesse Thaler, Steven Tsan, Silviu-Marian Udrescu, Louis Vaslin, Jean-Roch Vlimant, Daniel Williams, and Mikael Yunus. The lhc olympics 2020 a community challenge for anomaly detection in high energy physics. *Reports on Progress in Physics*, 84(12):124201, December 2021.
- [20] Jeong Han Kim, Kyoungchul Kong, Benjamin Nachman, and Daniel Whiteson. The motivation and status of two-body resonance decays after the lhc run 2 and beyond. *Journal of High Energy Physics*, 2020(4), April 2020.

- [21] Matteo Cacciari, Gavin P. Salam, and Gregory Soyez. The anti-k(t) jet clustering algorithm. *Journal of High Energy Physics*, 2008(04):063, 2008.
- [22] Jack H. Collins, Pablo Martín-Ramiro, Benjamin Nachman, and David Shih. Comparing weak- and unsupervised methods for resonant anomaly detection. *European Physical Journal C*, 81(7):617, 2021.
- [23] Jesse Thaler and Ken Van Tilburg. Identifying boosted objects with n-subjettiness. *Journal of High Energy Physics*, 2011(03):015, 2011.
- [24] Blaž Bortolato, Aleks Smolkovič, Barry M. Dillon, and Jernej F. Kamenik. Bump hunting in latent space. *Physical Review D*, 105(11):115009, 2022.
- [25] Tilman Plehn, Anja Butter, Barry Dillon, Theo Heimel, Claudius Krause, and Ramon Winterhalder. Modern machine learning for lhc physicists. *arXiv*, 2024.
- [26] Glen Cowan, Kyle Cranmer, Eilam Gross, and Ofer Vitells. Asymptotic formulae for likelihood-based tests of new physics. *Eur. Phys. J. C*, 71:1554, 2011. [Erratum: *Eur.Phys.J.C* 73, 2501 (2013)].
- [27] NOAA Physical Sciences Laboratory. Ncep-ncar reanalysis 1, 2024.
- [28] Sebastian Springer et al. Unsupervised detection of large-scale weather patterns in the northern hemisphere via markov state modelling: from blockings to teleconnections. *npj Climate and Atmospheric Science*, 7(105), 2024.
- [29] HD Brunk, James E Holstein, and Frederick Williams. The teacher’s corner: A comparison of binomial approximations to the hypergeometric distribution. *The American Statistician*, 22(1):24–26, 1968.
- [30] M. Tanner. Shorter signals for improved signal to noise ratio, the influence of poisson distribution. *Journal of Analytical Atomic Spectrometry*, 25:405–407, 2010.
- [31] Jason Gallicchio and Matthew D. Schwartz. Quark and Gluon Jet Substructure. *JHEP*, 04:090, 2013.



## Acknowledgements

AS was partially supported by the grant “DS4ASTRO: Data Science methods for Multi-Messenger Astrophysics & Multi-Survey Cosmology”, in the framework of the PRO3 ‘Programma Congiunto’ (DM n. 289/2021) of the Italian Ministry for University and Research. AL acknowledges foundations from NextGenerationEU through the Italian National Centre for HPC, Big Data, and Quantum Computing (Grant No. CN00000013). AL and SS also acknowledges financial support by the region Friuli Venezia Giulia (project F53C22001770002). RT and AS acknowledge funding from Next Generation EU, in the context of the National Recovery and Resilience Plan, Investment PE1 – Project FAIR “Future Artificial Intelligence Research”. This resource was co-financed by the Next Generation EU [DM 1555 del 11.10.22]. RT is partially supported by the Fondazione ICSC, Spoke 3 “Astrophysics and Cosmos Observations”, Piano Nazionale di Ripresa e Resilienza Project ID CN00000013 “Italian Research Center on High-Performance Computing, Big Data and Quantum Computing” funded by MUR Missione 4 Componente 2 Investimento 1.4: Potenziamento strutture di ricerca e creazione di “campioni nazionali di R&S (M4C2-19 )” - Next Generation EU (NGEU). MA acknowledges partial support from the UK Engineering and Physical Sciences Research Council [EP/W015080/1, EP/W522673/1]. MA also acknowledges partial support from the European Union’s Horizon 2020 research and innovation programme under European Research Council Grant Agreement No 101002652 (PI K. Mandel) and Marie Skłodowska-Curie Grant Agreement No 873089. HH was supported by the Research Council of Finland (RCoF) through the Flagship of advanced mathematics for sensing, imaging and modelling, decision number 358 944. GC is supported by the European Union’s Horizon Europe research and innovation programme under the Marie Skłodowska-Curie Postdoctoral Fellowship Programme, SMASH co-funded under the grant agreement No. 101081355. The operation (SMASH project) is co-funded by the Republic of Slovenia and the European Union from the European Regional Development Fund.

## Contribution statement

**Conceptualization:** S.S., A.L., and H.H. conceived the study and defined the initial scope of `EagleEye`, with S.S. serving as the primary author.

**Methodology:** All authors contributed to developing the methodology. S.S., H.H., and A.L. formulated the anomaly score framework—with M.A. and G.C. specifically distinguishing over- and underdensities. S.S. and A.L. designed the IDE and *Repêchage*, while M.A. and R.T. devised the background injection scheme. M.A., A.S., and G.C. designed the signal purity estimation.

**Software:** S.S. and A.S. implemented the `EagleEye` code.

**Experimental Design and Analysis:** A.S. led the LHC test case with support from G.C., R.T., and M.A., whereas S.S. led the climate test case in collaboration with A.L. and H.H. Extensive numerical experiments and subsequent refinements of the results and methods were carried out by S.S., A.S., M.A., and G.C.

**Visualization:** S.S., A.S., and G.C. prepared the figures with detailed input from all authors.

**Writing:** All authors discussed the results and collectively contributed to writing the manuscript.

## Supplementary Information

Here, we provide additional information regarding the methodology, analyses and results presented in the main text. The Supplementary Information is organised into three sections: the first provides technical details of our new methodology, along with additional background context; the section second focuses on sensitivity analyses using the Gaussian data considered in Sec. 3.1, exploring the impact of anomaly characteristics such as scale and placement, data volume, and dimensionality on `EagleEye`’s performance; and the third section examines the application of `EagleEye` to the LHC Olympics *R&D* dataset in Sec. 3.2, describing a two-sample test conducted to assess `EagleEye`’s sensitivity to rejecting the null (background-only) hypothesis. This section also briefly discusses an alternative metric used in the literature for benchmarking anomaly detection methods, as well as their limitations in a real-world, unsupervised setting.

## Methodology: Technical additions

The model described in Section 2 is a useful approximation rather than an exact representation. While the test statistic  $B(i, K)$  is modelled as a binomial distribution under the null hypothesis, the actual process follows a hypergeometric distribution because the nearest neighbours are selected without replacement from the combined set  $\mathcal{U}$ . The binomial distribution serves as an excellent approximation when the total number of points  $n_1 + n_2$  is large relative to  $K$ , ensuring that the difference between the two distributions becomes negligible in practice [29]. To maintain a good approximation, we set  $K_M$  to at most 5% of the data size, as recommended in the literature. In addition, we note that using independent Bernoulli trials to determine the critical thresholds  $\Upsilon_{\pm}^*$  is a practical approximation. Ideally, thresholds should be computed from multiple reference samples, but this is often unfeasible due to limited reference data. We have tested that this approximation works well, and the method remains robust to moderate threshold variations.

# Gaussian Density Anomalies in a Uniform Background: Anomaly detection sensitivity study

Below we provide a detailed sensitivity study pertaining to the multimodal Gaussian anomalies introduced in Sec. 3.1. We investigate the effect on the results after altering values of the hyperparameters  $K_M$  and  $\Upsilon_+^*$  (or, equivalently,  $p_{\text{ext}}$ ).

## Sensitivity with respect to variations in the maximum neighbourhood rank $K_M$

	$\mathcal{Y}_{\alpha=0}$	$\mathcal{Y}_{\alpha=1}$	$\mathcal{Y}_{\alpha=2}$	$\mathcal{Y}_{\alpha=3}$	$\mathcal{Y}_{\alpha=4}$	$\mathcal{Y}_{\alpha=5}$	$\mathcal{Y}_{\alpha=6}$	$\mathcal{X}_{\alpha=0}$	$\mathcal{X}_{\alpha=1}$	$\mathcal{X}_{\alpha=2}$
<b>Contamination:</b>	50 (50)	100 (100)	200 (200)	300 (300)	500 (500)	700 (700)	900 (900)	100 (100)	300 (300)	700 (700)
<b>Flagged:</b> $\hat{\mathcal{Y}}^+$	84 (50)	155 (100)	286 (200)	436 (300)	675 (499)	930 (696)	1180 (892)	200 (100)	462 (300)	796 (700)
<b>Pruned:</b> $\hat{\mathcal{Y}}^+$	54 (50)	69 (68)	135 (131)	230 (217)	354 (332)	515 (478)	654 (583)	89 (72)	295 (290)	705 (700)
$\mathcal{Y}_{\alpha}^{\text{anom}}$	83 (50)	93 (92)	208 (194)	322 (287)	535 (471)	728 (638)	1048 (849)	143 (99)	311 (300)	713 (700)
<b>Injected:</b> $\mathcal{Y}_{\alpha}^{\text{inj}}$	33	6	19	28	66	99	190	19	6	15

Table 3: Table illustrating the sensitivity of the results in Figure 2 to variations of the  $K_M$  hyperparameter. In this example, we set  $K_M = 300$  and obtain  $\Upsilon_+^* = 13.96$  ( $p_{\text{ext}} = 10^{-5}$ ). The first seven columns correspond to the  $\mathcal{Y}$ -overdensities, while the last three columns represent the  $\mathcal{X}$ -overdensities. The first row shows the number of points added to generate each anomaly (with the subset remaining at each phase given in parentheses). The subsequent rows list, respectively, the numbers of elements flagged as putative anomalies, pruned by IDE, and obtained via the Repêchage. Finally, the last row indicates the number of background elements estimated by the injection procedure.

	$\mathcal{Y}_{\alpha=0}$	$\mathcal{Y}_{\alpha=1}$	$\mathcal{Y}_{\alpha=2}$	$\mathcal{Y}_{\alpha=3}$	$\mathcal{Y}_{\alpha=4}$	$\mathcal{Y}_{\alpha=5}$	$\mathcal{Y}_{\alpha=6}$	$\mathcal{X}_{\alpha=0}$	$\mathcal{X}_{\alpha=1}$	$\mathcal{X}_{\alpha=2}$
<b>Contamination:</b>	50 (50)	100 (100)	200 (200)	300 (300)	500 (500)	700 (700)	900 (900)	100 (100)	300 (300)	700 (700)
<b>Flagged:</b> $\hat{\mathcal{Y}}^+$	96 (50)	178 (100)	365 (200)	568 (300)	863 (500)	1101 (700)	1434 (899)	235 (100)	694 (300)	908 (700)
<b>Pruned:</b> $\hat{\mathcal{Y}}^+$	52 (50)	69 (68)	153 (149)	230 (214)	379 (355)	530 (492)	692 (622)	86 (70)	295 (290)	696 (695)
$\mathcal{Y}_{\alpha}^{\text{anom}}$	63 (50)	93 (92)	211 (194)	311 (283)	531 (469)	792 (665)	1102 (872)	146 (99)	309 (300)	702 (700)
<b>Injected:</b> $\mathcal{Y}_{\alpha}^{\text{inj}}$	15	6	19	30	68	134	233	22	10	3

Table 4: Table illustrating the sensitivity of the results in fig. 2 to variations of the  $K_M$  hyperparameter. In this example, we set  $K_M = 700$  and obtain  $\Upsilon_+^* = 14.42$  ( $p_{\text{ext}} = 10^{-5}$ ).

## Sensitivity with respect to variations in the hyperparameter $\Upsilon_+^*$

	$\mathcal{Y}_{\alpha=0}$	$\mathcal{Y}_{\alpha=1}$	$\mathcal{Y}_{\alpha=2}$	$\mathcal{Y}_{\alpha=3}$	$\mathcal{Y}_{\alpha=4}$	$\mathcal{Y}_{\alpha=5}$	$\mathcal{Y}_{\alpha=6}$	$\mathcal{X}_{\alpha=0}$	$\mathcal{X}_{\alpha=1}$	$\mathcal{X}_{\alpha=2}$
<b>Contamination:</b>	50 (50)	100 (100)	200 (200)	300 (300)	500 (500)	700 (700)	900 (900)	100 (100)	300 (300)	700 (700)
<b>Flagged:</b> $\hat{\mathcal{Y}}^+$	103 (50)	175 (100)	331 (200)	519 (300)	782 (500)	1022 (699)	1338 (899)	238 (100)	619 (300)	866 (700)
<b>Pruned:</b> $\hat{\mathcal{Y}}^+$	54 (50)	69 (68)	153 (149)	240 (223)	380 (357)	535 (496)	687 (605)	91 (72)	295 (290)	702 (699)
$\mathcal{Y}_{\alpha}^{\text{anom}}$	92 (50)	93 (92)	211 (194)	309 (282)	537 (472)	671 (611)	1072 (861)	150 (100)	309 (300)	704 (700)
<b>Injected:</b> $\mathcal{Y}_{\alpha}^{\text{inj}}$	50	6	19	25	67	86	211	31	10	5

Table 5: Table illustrating the sensitivity of the results in fig. 2 to variations of the  $\Upsilon_+^*$  hyperparameter. In this example, we set  $K_M = 500$  and obtain  $\Upsilon_+^* = 12.61$  ( $p_{\text{ext}} = 5 \cdot 10^{-5}$ ).

	$\mathcal{Y}_{\alpha=0}$	$\mathcal{Y}_{\alpha=1}$	$\mathcal{Y}_{\alpha=2}$	$\mathcal{Y}_{\alpha=3}$	$\mathcal{Y}_{\alpha=4}$	$\mathcal{Y}_{\alpha=5}$	$\mathcal{Y}_{\alpha=6}$	$\mathcal{X}_{\alpha=0}$	$\mathcal{X}_{\alpha=1}$	$\mathcal{X}_{\alpha=2}$
<b>Contamination:</b>	50 (50)	100 (100)	200 (200)	300 (300)	500 (500)	700 (700)	900 (900)	100 (100)	300 (300)	700 (700)
<b>Flagged:</b> $\hat{\mathcal{Y}}^+$	91 (50)	167 (100)	326 (200)	507 (300)	770 (500)	1015 (699)	1320 (897)	227 (100)	608 (300)	862 (700)
<b>Pruned:</b> $\hat{\mathcal{Y}}^+$	52 (50)	69 (68)	153 (149)	230 (214)	359 (338)	526 (490)	669 (588)	89 (72)	295 (290)	702 (699)
$\mathcal{Y}_{\alpha}^{\text{anom}}$	62 (50)	93 (92)	211 (194)	308 (281)	537 (472)	688 (610)	1072 (861)	146 (99)	309 (300)	704 (700)
<b>Injected:</b> $\mathcal{Y}_{\alpha}^{\text{inj}}$	11	6	19	25	67	85	211	22	10	5

Table 6: Table illustrating the sensitivity of the results in fig. 2 to variations of the  $\Upsilon_+^*$  hyperparameter. In this example, we set  $K_M = 500$  and obtain  $\Upsilon_+^* = 14.04$  ( $p_{\text{ext}} = 10^{-5}$ ).

	$\mathcal{Y}_{\alpha=0}$	$\mathcal{Y}_{\alpha=1}$	$\mathcal{Y}_{\alpha=2}$	$\mathcal{Y}_{\alpha=3}$	$\mathcal{Y}_{\alpha=4}$	$\mathcal{Y}_{\alpha=5}$	$\mathcal{Y}_{\alpha=6}$	$\mathcal{X}_{\alpha=0}$	$\mathcal{X}_{\alpha=1}$	$\mathcal{X}_{\alpha=2}$
<b>Contamination:</b>	50 (50)	100 (100)	200 (200)	300 (300)	500 (500)	700 (700)	900 (900)	100 (100)	300 (300)	700 (700)
<b>Flagged:</b> $\hat{\mathcal{Y}}^+$	90 (50)	166 (100)	324 (200)	504 (300)	770 (500)	1013 (699)	1319 (897)	226 (100)	608 (300)	862 (700)
<b>Pruned:</b> $\hat{\mathcal{Y}}^+$	52 (50)	69 (68)	153 (149)	230 (214)	359 (338)	524 (488)	669 (588)	86 (70)	295 (290)	702 (699)
$\mathcal{Y}_{\alpha}^{\text{anom}}$	62 (50)	93 (92)	211 (194)	308 (281)	537 (472)	688 (610)	1072 (861)	146 (99)	309 (300)	704 (700)
<b>Injected:</b> $\mathcal{Y}_{\alpha}^{\text{inj}}$	11	6	19	25	67	85	211	22	10	5

Table 7: Table illustrating the sensitivity of the results in fig. 2 to variations of the  $\Upsilon_+^*$  hyperparameter. In this example, we set  $K_M = 500$  and obtain  $\Upsilon_+^* = 14.31$  ( $p_{\text{ext}} = 5 \cdot 10^{-6}$ ).

# Anomalies within a 10D Gaussian Background: Sensitivity to Reference Set Morphology and Cardinality

In order to evaluate the robustness of our detection procedure in high-dimensional settings under varying background conditions, we consider two experimental scenarios, which we denote 1) and 2) respectively (see below). For each study 1) and 2) we consider two anomaly morphologies:

- **Torus Anomaly:** For each anomalous point, the first three components are drawn uniformly from a torus with a major radius  $R_a = \sigma_a$  and a minor radius  $r_a = R_a/6$ , while the remaining seven components are sampled from  $\mathcal{N}(0, \sigma_a)$ .
- **Gaussian Anomaly:** All components of each anomalous point are drawn from  $\mathcal{N}(0, \sigma_a)$ .

In both of the above cases, the characteristic scale is set to  $\sigma_a = 0.3$ .

The below examples demonstrate a key conclusion of **EagleEye**, which is that local anomaly detection is directly dependent only on *local density variations*, and not on extensive changes in cardinality and/or morphology of the data space, as long as local density differences are preserved.

**1) Impact of Increased Cardinality with Altered Local Density** In this scenario, the background sample size  $|B|$  is increased by an order of magnitude. Consequently, the anomalous points in the test set become more diluted, simultaneously resulting in an increased cardinality of the repêchage set,  $|\mathcal{Y}_{\alpha=1}^{\text{anom}}|$ .

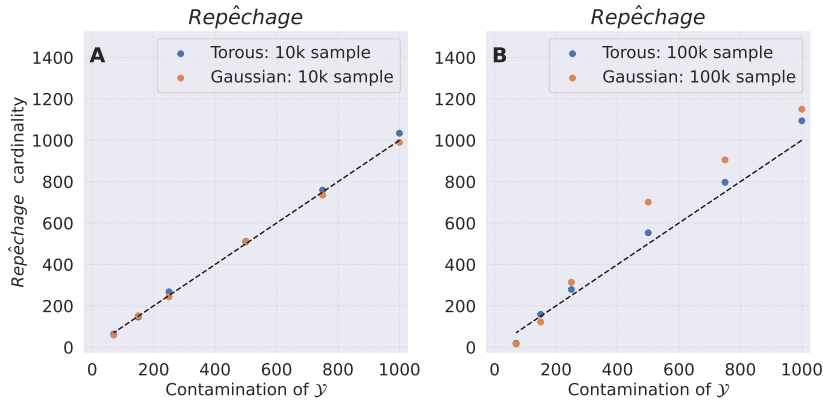


Figure 5: Variation in the cardinality of the repêchage sets (vertical axis) as a function of the number of contaminating points (horizontal-axis) in the test set  $\mathcal{Y}$ . Here, the maximum neighbourhood rank is set to  $K_M = 500$  and the default  $p_{ext} = 10^{-5}$  is used. Panel A corresponds to datasets of 10,000 test and reference points, whereas Panel B shows datasets of 100,000 points, where the additional 90,000 points are drawn from the same underlying Gaussian distribution.

**2) Impact of Increased Cardinality with Unaltered Local Density** In the second scenario, the background is augmented by sampling additional points from a separate Gaussian mixture. This strategy preserves the local density contrast between the anomalies and the background, thereby maintaining stable detection performance despite the increased overall cardinality.

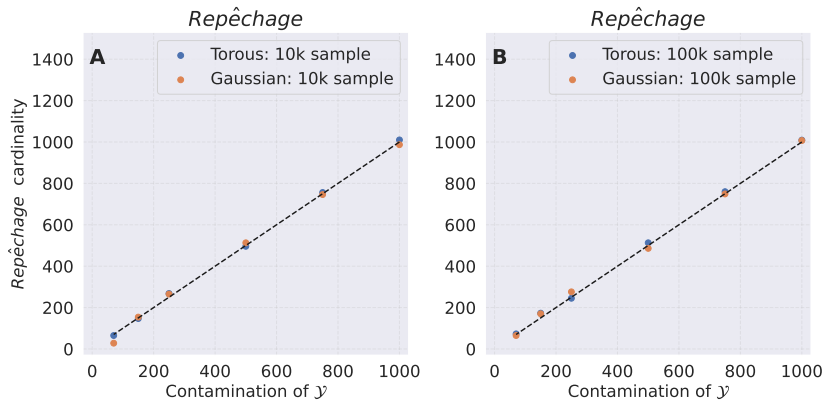


Figure 6: Variation in the size (cardinality) of the resulting sets (vertical-axis) as a function of the number of contaminating points (horizontal-axis). With  $K_M = 500$  and the default  $p_{ext}$ , Panel A illustrates the scenario for 10,000-point datasets, while Panel B corresponds to 100,000-point datasets. In this case, the additional 90,000 points are now drawn from *six* Gaussian modes arranged around the primary mode, forming a petal-like structure.

## Underdensities within a Uniform 3D Background

To illustrate that the introduction of  $\mathcal{X}$ -overdensities in Fig. 2 is equivalent to removing test points from a particular region of the feature space and reallocating them elsewhere, we consider a simplified scenario. Here, the reference dataset comprises 50,000 points uniformly sampled in 3D over the interval  $[-1, 1]$ . An underdensity is generated by reassigning, with a probability of 90%, those test set points located within a sphere of radius 0.2 centered at the origin to a new position within the uniform background. The analysis of this scenario, presented in Fig. 7, confirms that our method can reliably detect underdensities even when only a modest fraction of points is perturbed in the test dataset.

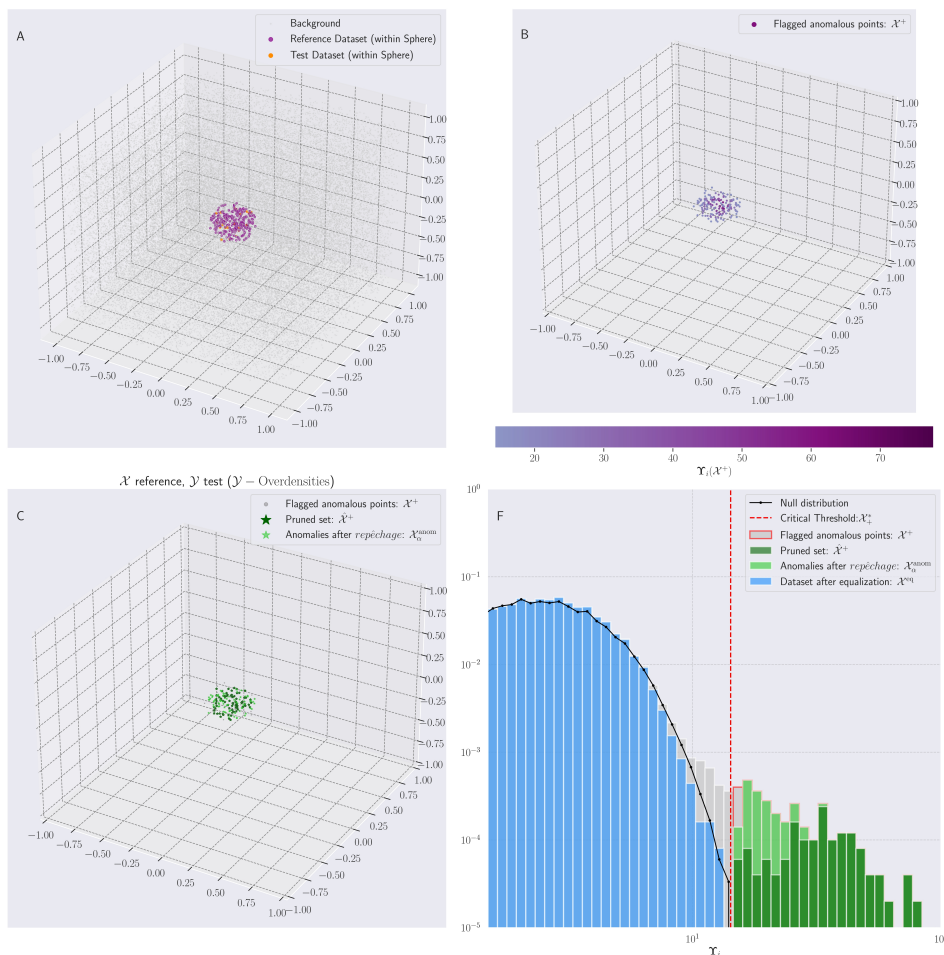


Figure 7: **EagleEye** detection of density anomalies within a uniform background. **(A)**: distribution of anomalies in feature space, showing underdensities (violet). **(B)**: Scatter plots of points flagged as anomalous in the reference set (cool violet shades). **(D)**: Local anomalies after Iterative Density Equalization (dark green) and multimodal repêchage (light green). On the left, overdensities, on the right, underdensities. **(F)**: Distribution of the anomaly score  $\Upsilon_i$  for sequences of Bernoulli trials (black, null distribution); the test set (gray), the pruned set (dark green); the clustered anomaly set (light green), and the equalized set (blue, matching the null distribution).

## Derivation of the signal-to-background ratio estimator:

As defined in Sec. 2.4:

$$S_\alpha + B_\alpha = |\mathcal{Y}_\alpha^{\text{anom}}| \quad (10)$$

$$\Rightarrow \frac{S_\alpha}{S_\alpha + B_\alpha} = \frac{|\mathcal{Y}_\alpha^{\text{anom}}| - B_\alpha}{|\mathcal{Y}_\alpha^{\text{anom}}|}$$

The number of background samples in the anomalous test region  $\alpha$ ,  $B_\alpha$ , is of course not known. However, we know that the test background  $B_y$  and the reference background  $B_x$  share the same distribution.  $B_y$  is the non-anomalous test component, and  $B_x$  is the non-anomalous component of the reference set.

Via the injection scheme we obtain the following (in expectation):

$$\frac{B_\alpha}{B_y} = \frac{|\mathcal{Y}_\alpha^{\text{inj}}|}{B_x}$$

and thus

$$B_\alpha = \frac{|\mathcal{Y}_\alpha^{\text{inj}}|}{B_x} B_y$$

We can estimate the size of the test background component  $B_y$  by subtracting the estimated size of the test overdensities from the total test size, i.e.

$$B_y \approx n_y - |\hat{\mathcal{Y}}^+|$$

The size of the reference background component  $B_x$  can be estimated by subtracting the estimated size of the reference overdensities from the total reference size, i.e.,

$$B_x \approx n_x - |\hat{\mathcal{X}}^+|$$

Leading to the estimation:

$$\frac{\widehat{S_\alpha}}{S_\alpha + B_\alpha} = \frac{|\mathcal{Y}_\alpha^{\text{anom}}| - \left( |\mathcal{Y}_\alpha^{\text{inj}}| \frac{(n_y - |\hat{\mathcal{Y}}^+|)}{(n_x - |\hat{\mathcal{X}}^+|)} \right)}{|\mathcal{Y}_\alpha^{\text{anom}}|}$$

We additionally provide an estimate of the quantity  $S/\sqrt{B}$ , which has the additional property of estimating the statistical significance of a Poisson process [26, 30]. The derivation follows as above, making the appropriate substitution for  $\sqrt{B_\alpha}$  in the denominator:

$$\frac{\widehat{S_\alpha}}{\sqrt{B_\alpha}} = \frac{|\mathcal{Y}_\alpha^{\text{anom}}| - \left( |\mathcal{Y}_\alpha^{\text{inj}}| \frac{(n_y - |\hat{\mathcal{Y}}^+|)}{(n_x - |\hat{\mathcal{X}}^+|)} \right)}{\sqrt{|\mathcal{Y}_\alpha^{\text{inj}}| \frac{(n_y - |\hat{\mathcal{Y}}^+|)}{(n_x - |\hat{\mathcal{X}}^+|)}}}. \quad (11)$$

## LHC Olympics: Rejecting the standard model (background-only) interpretation in the presence of small anomalous signal injection.

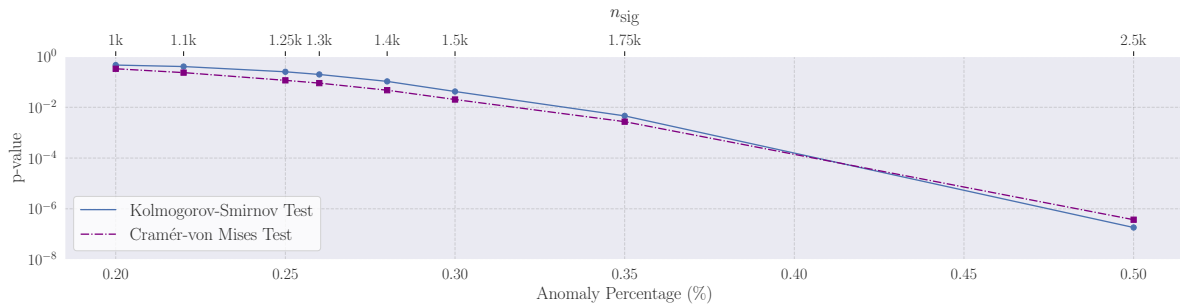


Figure 8: **Global detection of anomalies in the LHC Olympics R&D dataset.** The  $p$ -values from a two-sample Kolmogorov-Smirnov test (blue solid lines with circular markers) and a two-sample Cramér-von Mises test (purple dash-dotted lines with circle markers) on the distribution of anomaly scores  $\Upsilon_i$ , applied to the LHC Olympics R&D dataset, plotted as a function of the fraction of contaminant anomalous points. The top axis shows the number of anomalous events added ( $n_{\text{sig}}$ , for signal events), corresponding to the percentages on the bottom axis.

In high energy physics, it is often of primary scientific importance to obtain a global statistical significance test for rejecting the null hypothesis of background only, i.e., for detecting the presence of *any* non-standard model events. To this end, we used the two-sample Kolmogorov-Smirnov (KS) test and the Cramér-von Mises (CVM) test, to explicitly test the similarity between the distribution of anomaly scores,  $\Upsilon_i$ , obtained for the test dataset and reference dataset where the 'null' distribution is a withheld subsample of the reference dataset (corresponding to zero signal percentage). We have checked that this observed null distribution and the Bernoulli trials distributions agree as expected. This one-dimensional test is diagrammatically represented as a comparison between the black line and the grey distribution in Figure 3; If no density anomalies are present, the distribution of  $\Upsilon_i$  corresponding to the sets  $\mathcal{Y}^+$  and  $\mathcal{X}^+$  should not significantly deviate from the distribution of  $\Upsilon_i$  obtained from a test set comprising of no signal.

We perform the two-sample tests for varying anomaly contamination fractions, in the range  $\in [0.2, 0.5]\%$ . The results are shown in Fig. 8 as the blue points (KS test) and purple points (CVM test). The KS-test and CVM achieve  $p$ -values of 0.04 and 0.02 respectively for signal percentages of 0.3%. We cut off at an anomaly percentage of  $> 0.5\%$  as displaying the results then becomes difficult due to exponentially decreasing  $p$ -values.

We caution that it is still possible for **EagleEye** to detect local anomalies in feature space even when a global null-rejection test as proposed above, fails to measure a significant deviation in the distribution of  $\Upsilon_i$ . We display such a contrived scenario in Fig. 9. We therefore caution the reader that such global tests may be useful in quantifying the presence of *any* anomaly in the data, but that a non-significant (i.e., large) global  $p$ -value obtained from the KS or CVM test does not imply that **EagleEye** cannot detect a local density anomaly.

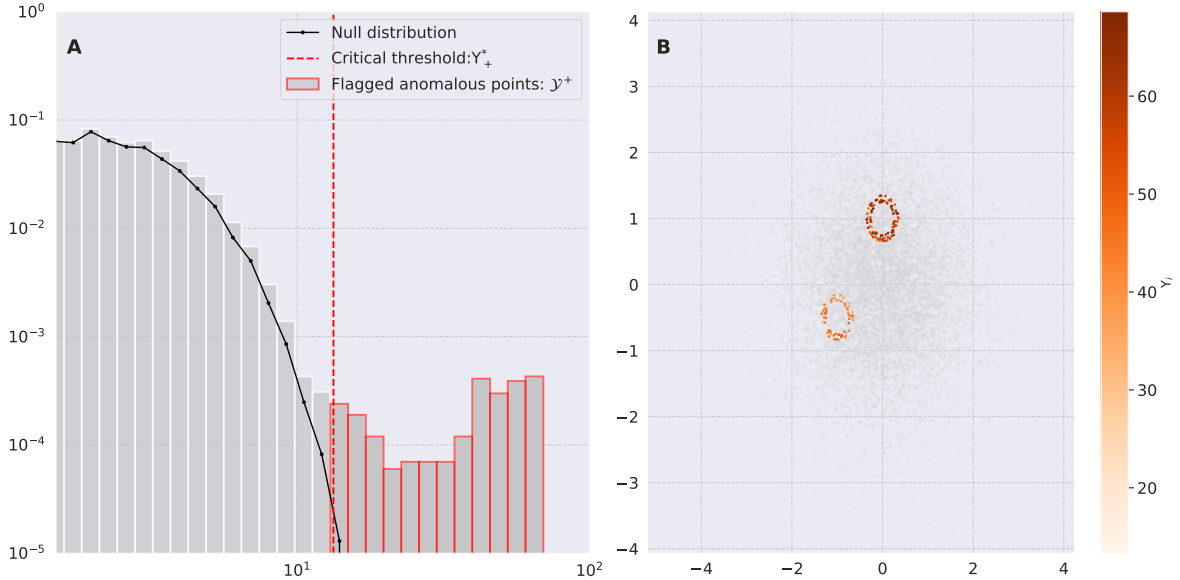


Figure 9: FIX ME! I’ll do it from the office on friday as it looks nicer when done on a bigger schreen. **Global significance tests for the presence of anomalies.** This figure demonstrates that standard global significance tests may fail to detect anomalies that are however correctly identified and localised by **EagleEye**. The reference dataset consists of 100,170 samples from a 10-dimensional standard Gaussian distribution. The test dataset includes, on top of 10,000 points drawn from the same 10-dimensional standard Gaussian. two torus-shaped clusters, one comprising 100 points and the other 70 points added in the first three components; the remaining components are Gaussian with adjusted standard deviations to match the torus components. The maximum neighbourhood size  $K_M$  has been set at 100. **A:** Histogram of  $\Upsilon_i$  for the test dataset. The black line represents the distribution of  $\Upsilon_i$  generated from sequences of Bernoulli trials, used to establish the critical threshold displayed as a dashed vertical line. **B:** Scatter plot of the test dataset, with points colour-coded according to their  $\Upsilon_i$  values, highlighting regions with higher anomaly scores. Standard two-sample tests for rejecting the null hypothesis that the two datasets come from the same distribution give a non-significant result:  $p$ -values of 0.7 and 0.59 are obtained for the KS and CVM tests respectively. We additionally perform an Anderson-Darling test which places more emphasis on the tails of the distributions, still only yielding a  $p$ -vale of 0.11.

## LHC Olympics: Comparison with standard benchmark metrics

Several metrics are used in the literature for assessing the “global significance” of anomalies in the LHC Olympics R&D dataset. Most approaches use the significance improvement characteristic (SIC) curve [25, 31], which describes the enhancement of  $S/\sqrt{B}$  due to the classifier’s threshold choice within a signal region. Density estimation methods like CATHODE and ANODE explicitly rely on the definition of such a signal region and its so-called ‘sideband’—regions expected to consist only of background (as control regions and for calibration purposes).

In contrast, **EagleEye** does not apply any cuts in feature space. As such, we emphasise that our benchmark analysis is intended to be as agnostic as possible to a potential signal, replicating what one might obtain in a real unsupervised study. Furthermore, the key innovation of **EagleEye** lies in its ability to identify *the locations* of flagged anomalies within the feature space. Therefore, a fair quantitative comparison of **EagleEye**’s performance with other methods would require a metric that includes a measure of localisation of the anomaly, which is not available.

With the above caveat, we provide an approximate comparison to current cutting-edge methods by calculating the Maximum Achieved Significance (MAS), defined as:

$$\text{MAS} = \max_{\Psi} \left[ \left( \frac{S}{\sqrt{B}} \right)^{\text{Truth}} (\Psi) \right],$$

where  $\Psi$  denotes the threshold used by an anomaly detection method to classify a point as  $S$  or  $B$  (in our case, we take  $\Psi = \Upsilon_+^*$ ). The MAS corresponds to the value of  $S/\sqrt{B}$  when the SIC is maximised over the classifier threshold. In Table 2 in the main text, we report the ‘Total’  $\frac{S_{\alpha}^{\text{Truth}}}{\sqrt{B_{\alpha}}}$ , which corresponds to the signal-to-background ratio obtained from  $\bigcup_{\alpha} \mathcal{Y}_{\alpha}^{\text{anom}}$  and  $\bigcup_{\alpha} \mathcal{Y}_{\alpha}^{\text{inj}}$ , for our fixed choice of  $\Upsilon_+^*$ . In order to then match the approach used in the right plot of Figure 7 in Ref. [7], we must optimize the threshold  $\Upsilon_+^*$  in order to calculate the MAS. We note that the choice of  $\Upsilon_+^*$  that was used in Section 3.2, chosen to approximately maximise  $\widehat{\frac{S_{\alpha}}{\sqrt{B_{\alpha}}}}$ , was also seen to approximately obtain the MAS. Therefore, the values of  $\frac{S_{\alpha}^{\text{Truth}}}{\sqrt{B_{\alpha}}}$  reported in Table 2 remain suitable for comparison. With the above caveats, **EagleEye** achieves a MAS of 5.75 for an anomaly

injection percentage (in the entire data space) of 0.3%, and 23.0 for 0.5%, compared with CATHODE which achieves a MAS of  $\sim 5.7$  and  $\gtrsim 20$ , respectively, ANODE (MAS  $\sim 4$  and  $\sim 10$ , respectively) and CWoLa (MAS  $\sim 3$  and 12.5, respectively). All the comparators values are defined with respect to their signal region only.

An alternative comparison is obtained by imposing the same signal region cuts as in Ref. [7], and then applying **EagleEye** only to the points in the signal region. These cuts yield approximately  $6 \times 10^4$  background points from our initial background reference set of  $5 \times 10^5$ . For a signal percentage of 0.3% inside such a signal region, that would give just 180 signal points, which is insufficient for **EagleEye** to give a reliable density estimation. One would have to resort to a larger number of Monte Carlo simulations initially, which are not available to us (though in principle can be produced). To circumvent this issue, we resampled the reference set with small Gaussian perturbations added to each data corresponding to some small fraction ( $\sim 10^{-2}$ ) of each features' variance. This resulted in an augmented set of points encompassing  $\sim 6 \times 10^5$  background and  $\sim 1900$  signal points. Although this strategy does not fully replicate a complete Monte Carlo simulation, it still effectively captures the number of neighbours responsible for contributing to the background in the area of a local overdensity. We find that in this case the MAS obtained with **EagleEye** remains similar ( $\gtrsim 5.5$ ) to that obtained without signal region cuts.